Lamellipodin tunes cell migration by stabilizing protrusions and promoting adhesion formation

Georgi Dimchev[1,2], Behnam Amiri[3], Ashley C. Humphries[4,7], Matthias Schaks[1,2], Vanessa Dimchev[1,2], Theresia E.B. Stradal[2], Jan Faix[5], Matthias Krause[6], Michael Way[4], Martin Falcke[3,*], and Klemens Rottner[1,2,8,*]

[1]Division of Molecular Cell Biology, Zoological Institute, Technische Universität Braunschweig, Spielmannstrasse 7, 38106 Braunschweig, Germany; [2]Department of Cell Biology, Helmholtz Centre for Infection Research, Inhoffen Strasse 7, 38124 Braunschweig, Germany; [3]Max Delbrück Center for Molecular Medicine, Robert Rössle Strasse 10, 13125 Berlin, Germany; [4]Cellular Signalling and Cytoskeletal Function Laboratory, The Francis Crick Institute, London, England, UK; [5]Institute for Biophysical Chemistry, Hannover Medical School, Carl-Neuberg-Strasse 1, 30625 Hannover, Germany; [6]Randall Centre of Cell & Molecular Biophysics, King's College London, New Hunt's House, Guy's Campus, London, SE1 1UL, UK; [8]Braunschweig Integrated Centre of Systems Biology (BRICS), Braunschweig, D-38106, Germany

[7]**present address:** Icahn School of Medicine at Mount Sinai, New York, USA

[*]**Authors for correspondence:** Klemens Rottner or Martin Falcke

Klemens Rottner: Phone: +49 531 391 3255, Email: k.rottner@tu-braunschweig.de

Martin Falcke: Phone: +49 30 9406 2753, Email: martin.falcke@mdc-berlin.de

Running title: Lamellipodin function in protrusion

Key words: lamellipodium, VASP, Arp2/3, WAVE regulatory complex

Summary statement: We describe how genetic ablation of the prominent actin- and VASP-binding protein lamellipodin combined with software-aided protrusion analysis uncovers mechanistic insights into its cellular function during cell migration.

ABSTRACT

Efficient migration on adhesive surfaces involves the protrusion of lamellipodial actin networks and their subsequent stabilization by nascent adhesions. The actin binding protein lamellipodin (Lpd) is thought to play a critical role in lamellipodium protrusion, by delivering Ena/VASP proteins onto the growing barbed ends of actin filaments and by interacting with the WAVE regulatory complex (WRC), an activator of the Arp2/3 complex, at the leading edge. Using B16-F1 melanoma cell lines, we found that genetic ablation of Lpd compromises protrusion efficiency without altering essential lamellipodial parameters, including their maximal rate of forward advancement and actin polymerization. Consistently, interference with Lpd function also decreases the frequency of Vaccinia actin tail formation, but not their speed. Moreover, computer-aided analysis of cell edge morphodynamics revealed that loss of Lpd correlates with reduced temporal maintenance of lamellipodial protrusions as a prerequisite of nascent adhesion formation. We conclude that Lpd optimizes protrusion and nascent adhesion formation by counteracting frequent, chaotic retraction and membrane ruffling.

INTRODUCTION

The protrusion of cell surface projections such as lamellipodia and filopodia is crucial for various processes ranging from migration of individual, mesenchymal or tumour cells to neuronal growth cone advance or epithelial zippering as prerequisite, e.g., of adherens junction formation (Bachir et al., 2017; Omotade et al., 2017; Rottner et al., 2017). Lamellipodin (Lpd), a member of the Mig10/RIAM/Lpd family of adaptor proteins (MRL), localizes at the edges or tips of protruding lamellipodia and filopodia and interacts with multiple actin assembly factors involved in the regulation of dynamic actin remodelling events (Colo et al., 2012; Krause and Gautreau, 2014). Lpd supports lamellipodia protrusion and cell migration, to promote cancer cell invasion and neural crest migration. It also supports neuronal morphogenesis, endocytosis and localises to the interface of vaccinia viruses and their actin tails (Bodo et al., 2017; Carmona et al., 2016; Hansen and Mullins, 2015; Krause et al., 2004; Law et al., 2013; Vehlow et al., 2013). All these functions are mediated by individual lamellipodin domains, but we still need a better understanding of how Lpd functions via its respective binding partners. For example, plasma membrane localisation of Lpd is clearly facilitated by its pleckstrin homology (PH) domain, which enables interactions with PI(3,4)P2 membrane phospholipids (Bae et al., 2014; Krause et al., 2004; Smith et al., 2010a). Nevertheless, actin filament binding through C-terminal sequences lacking the PH-domain is necessary and sufficient for Lpd enrichment at the lamellipodium edge (Hansen and Mullins, 2015).

Lpd can regulate lamellipodia formation and cell migration through interactions with WAVE Regulatory Complex (WRC) (Law et al., 2013), a potent activator of the Arp2/3 complex (Rottner et al., 2017; Schaks et al., 2018), or with both WRC and Ena/VASP family proteins, dependent on cell system and conditions (Carmona et al., 2016; Krause and Gautreau, 2014; Krause et al., 2004). Lpd binds directly to the SH3-domain of the WRC subunit Abi, and this interaction is positively regulated by Rac binding to the Ras association (RA) domain of Lpd as well as by Src-dependent Lpd phosphorylation (Law et al., 2013). Moreover, the association

between Lpd and Ena/VASP proteins is regulated by Abl family kinases and occurs through its C-terminal Ena/VASP homology 1- (EVH1-) binding sites (Hansen and Mullins, 2015; Krause et al., 2004; Michael et al., 2010). The potential relevance of this interaction to lamellipodial dynamics is supported by the prominent accumulation of both Lpd and Ena/VASP proteins at the edges of protruding lamellipodia (Hansen and Mullins, 2015; Krause et al., 2004; Rottner et al., 1999). Mechanistically, the actin filament binding activity of Lpd, which can occur independently of Ena/VASP binding, was proposed to tether the latter to growing barbed ends, thereby increasing their processive polymerase activity (Hansen and Mullins, 2015).

Lpd promotes migration processes at multiple scales, ranging from neural crest-derived melanoblast migration in mice to border cell migration in *Drosophila* (Law et al., 2013). Through its Ena/VASP and WRC interactions, Lpd also increases cancer cell invasion, and its increased protein expression in breast cancer samples correlates with poor prognosis in breast cancer patients (Carmona et al., 2016). At the subcellular level, Lpd overexpression increases the speed of lamellipodia protrusion, while its knockdown by RNA interference (RNAi) impairs their formation (Carmona et al., 2016; Krause et al., 2004). However, the consequences of permanent loss of function of Lpd by its genetic ablation in growing cell lines could hitherto not be studied. Apart from aforementioned functions in lamellipodium protrusion and migration, Lpd has also been implicated in various additional processes either involving or at least impacting on actin dynamics. These processes include additional types of protrusion, such as those mediating cell-to-cell spreading of pathogenic *Listeria monocytogenes* (Wang et al., 2015), but also integrin activation through its binding to talin (Lagarrigue et al., 2015; Lee et al., 2009; Watanabe et al., 2008) or the fast endophilin-mediated endocytosis (FEME) pathway (Boucrot et al., 2015; Chan Wah Hak et al., 2018). How Lpd sorts to or is regulated within these distinct subcellular structures, remains to be investigated.

To this end, we generated permanent B16-F1 mouse melanoma cell lines genetically disrupted for Lpd by CRISPR/Cas9, to precisely determine the consequences of Lpd loss of function in

its complete absence. We also describe a novel cell edge analysis workflow that employs edge detection via ImageJ and quantitative, morphodynamic analysis, in order to retrieve a large number of parameters to reveal and compare complex cellular protrusion and retraction phenotypes. Our analysis reveals that while not essential, Lpd does help optimize protrusion at the leading edge, but without qualitatively or quantitatively affecting the rates of lamellipodial actin network polymerization. Instead, the loss of Lpd leads to changes in nascent adhesion number and distribution. We conclude that Lpd contributes to the efficiency of cell migration in part through coordinating actin dynamics with cell-substratum adhesion.

RESULTS

Genetic deletion of Lpd in B16-F1 melanoma cells reduces lamellipodial protrusion and rates of migration

In order to investigate the effects of eliminating Lpd expression on lamellipodial protrusion, we disrupted the *Lpd* gene in murine B16-F1 melanoma cells using CRISPR/Cas9. Multiple B16-F1 cell clones were isolated from the CRISPR/Cas9 transfection pool, of which 3 clones were randomly selected for further characterization (termed Lpd KO#3, #8 and #10). Immunoblot analyses with three distinct antibodies confirmed the absence of Lpd expression in selected cell lines (Fig. 1A, Fig. S1A, B). Sequencing of the target site locus also validated the lack of wildtype alleles in selected knockout lines (Fig. 1B). As observed previously for other genes in B16-F1 cell lines generated by CRISPR/Cas9 (Kage et al., 2017; Schaks et al., 2018), the Lpd knockout clones contained alleles with different numbers of frameshift mutations (up to 5 depending on clone) causing pre-mature stop codons shortly following the CRISPR target site in exon 5 (Fig. 1B). The sequencing results revealed that stop codons were induced just upstream of the RA-domain of Lpd. As a consequence, a potential truncated protein – if at all present - would be devoid of all major regulatory domains, including PH-domain as well as EVH1-, SH3- and F-actin binding sites, which are all located C-terminal of the RA-domain. In order to confirm the lack of a functional protein at the single cell level, immunofluorescence analysis with an antibody specific for the C-terminus of Lpd was performed, which revealed that the localization of Lpd at lamellipodia edges seen in wildtype B16-F1 cells (Krause et al., 2004) was absent in *Lpd* gene-disrupted cell lines (Fig. S1C). We also explored the expression of RIAM/PREL-1, the second member of the MRL (Mig-10, Riam and lamellipodin) family, but consistent with previous data (Jenzora et al., 2005), the protein was undetectable by Western Blotting in B16-F1 wildtype cells in contrast to NIH 3T3 fibroblasts (Fig. S1D). RIAM/PREL-1 was also not upregulated in our Lpd-deficient cell lines (Fig. S1E).

We observed that lamellipodia were still able to form in the absence of Lpd in our B16F1 CRISPR KO lines (Fig. S1C, see also below). To initially assess the impact of the loss of Lpd on lamellipodial dynamics, we performed a manual, kymography-based analysis, determining the protrusion and retraction behaviour in B16-F1 wildtype and Lpd-KO clones with or without expression of EGFP-Lpd over 5 minutes (Fig. 1C). This analysis already implied protrusion to be more irregular (Fig. 1C) and less efficient (Fig. 1D). Moreover, the reduction of protrusion was fully rescued by expression of EGFP-Lpd (Fig. 1C, D), confirming the observed phenotypes are solely dependent on Lpd. Lpd-EGFP expression in wildtype cells did not increase lamellipodial protrusion rates in a statistically significant fashion (Fig. 1D), suggesting that Lpd function in protrusions is saturated in this cell type. Since the efficiency of cell migration is highly dependent on lamellipodia in B16-F1 cells (Dolati et al., 2018; Schaks et al., 2018), we also examined random cell migration of our cell lines on laminin (Movie 1). Individual cell migration trajectory plots and corresponding quantifications reveals a moderate, statistically significant reduction in random migration rates in the absence of Lpd (Fig. 1E, F). This was also reflected by reduced mean square displacement of Lpd KO cells compared to wildtype controls (Fig. 1G). Together, our results reveal that B16-F1 cells lacking Lpd have reduced, but not eliminated lamellipodia protrusion activity and reduced cell migration efficiency.

Loss of Lpd induces a shift towards a chaotic lamellipodial phenotype

To uncover the basis for reduced lamellipodial protrusion upon Lpd deletion, we explored lamellipodial protrusion patterns in our cell lines in further detail. Not surprisingly, we observed that at any given time point, lamellipodial protrusion phenotypes can differ significantly between cells in the same population, and that lamellipodial dynamics can display heterogeneous patterns over time, even at the single cell level (Wang et al., 2018). To deal with the variability inherent in the system and to unambiguously display the heterogeneity in

morphodynamic cell edge behaviours, we used semi-automatic cell edge tracking in cell lines expressing plasma membrane-targeted CAAX-EGFP. To achieve this, we used an ImageJ-based plug-in called JFilament (Smith et al., 2010b), followed by quantitative analysis of lamellipodial morphodynamics (see Methods). The spatiotemporal evolution of tracked lamellipodial contours over representative time periods of 2 minutes reveals there are three basic types of lamellipodial protrusion classes designated as smooth, intermediate and chaotic phenotype within B16-F1 control and Lpd knockout cell populations (Fig. 2A). Lamellipodia corresponding to the smooth phenotype protruded in a steady and persistent manner. Lamellipodia of intermediate phenotype protruded in a fluctuating manner, and chaotic lamellipodia underwent rapid cycles of protrusion and retraction, with the cell edge frequently folding backwards. Velocity and curvature maps allow clear visualization of the spatiotemporal differences of tracked cell edges between the three protrusion classes, with spatial fluctuations in both parameters clearly increasing from smooth to chaotic over time (Fig. 2B, C and Movies 2 and 3).

Since we observed that Lpd knockout clones have a reduced average rate of lamellipodial protrusion, we investigated whether the fraction of cells for a given protrusion class is altered compared to B16-F1 controls. Analysis of movies reveals that the fraction of cells with smooth and intermediate protrusions were significantly reduced in Lpd-KO cells (> two times for smooth, Fig. 2D), whereas the chaotic class increased by a factor of 3.82 (Fig. 2D, also see Movie 1). These data show there is a clear correlation between Lpd expression and lamellipodial protrusion stability.

Lpd loss impacts on multiple morphodynamic parameters of lamellipodial protrusion

Software-aided, semi-automatic cell edge tracking and analysis allowed to define 20 parameters, 18 of which are arbitrarily separated into groups associated with protrusion-, retraction-, dynamics/velocity- or curvature/geometry-related characteristics of the cell edge

(for description of each parameter, see Table S1). The averaged and normalized values of these 20 parameters from B16-F1 wildtype *versus* Lpd KO cells are provided (for pooled data see Fig. 3 and individual clones Fig. S2). Multiple conclusions can be drawn from reviewing the 20 morphodynamic parameters in Figure 3. First, a significant reduction of *Average Advancement Velocity* (parameter #1) was observed in the absence of Lpd, confirming the results from the equivalent, manual, kymograph-based analysis (Fig. 1D). Aside from parameter #1, which considers both protrusion and retraction episodes, we also dissected protrusion and retraction events individually. This analysis indicates that Lpd knockout cells display reduced values of some, but not all, protrusion-related parameters including *Effective Protrusion* (parameter #2; Figs. 3 and S2). This parameter solely considers the rate of lamellipodial protrusion at the measured edge, without retraction, but averaged for the entire duration of acquisition (120 sec). Another parameter reduced in a statistically significant fashion by loss of Lpd is the *Protruding Edge Fraction* (parameter #3), which reports how many pixels analysed periphery spend protruding. The reduction in parameters 2 and 3 reveals that lamellipodial protrusion activity in the absence of Lpd is compromised not only by the effective, average rate of protrusion, but also the percentage of cell periphery capable of protruding at any given time. We also found that Lpd knockout cells display reduced average velocity during individual protrusion episodes (*Protrusion Episode Velocity*, parameter #5). The difference in values obtained from this parameter, however, is subtler than those for *Average Advancement Velocity* (parameter #1) and *Effective Protrusion* (parameter #2). Furthermore, when maximal protrusion rates are displayed (*Maximal Velocity during Protrusion*, parameter #6), it becomes evident that Lpd knockout cells can transiently reach the same protrusion speed as B16-F1 controls, although this rate is not maintained as efficiently as in the presence of Lpd, explaining reductions observed in protrusion-related parameters #2-5.

Our analysis of *Average Advancement Velocity* (parameter #1) in cells lacking Lpd reveals it is also influenced by retraction-related parameters (#7-11), as their average values are all

increased in the absence of Lpd. This then contributes to the observation that the *Retraction to Protrusion Ratio* (parameter #12) is significantly increased in Lpd knockout cells as compared to controls. Furthermore, examination of the dynamics of lamellipodia reveals that relative to B16-F1 controls, Lpd KO cells, on average, tend to display more frequent membrane oscillations/fluctuations (*Frequency of Oscillations*, parameter #13) and velocity changes (*Variance of Edge Acceleration*, parameter #14), and have stronger and less predictable fluctuations (parameters #15 and #16, respectively). In spite of this variability in velocity-related features, curvature-related parameters indicated that the leading edges of Lpd knockout cells have longer concave and convex segments (parameters #17 and #18), caused by the fact that changes of curvature profile over time (*Curvature Change over Time*, parameter #19) and along the edge (*Curvature Variability along Edge*, parameter #20) are strongly reduced in the absence of Lpd. All these data suggest that Lpd also contributes to local flexibility and plasticity of cell edge protrusion.

Focusing on individual morphodynamic parameters allows drawing specific conclusions on how individual aspects of lamellipodial protrusion, retraction, dynamics or geometry differ between Lpd knockout and wildtype cells. However, analysis of the individual parameters does not uncover the precise quantitative contributions of all protrusion- *versus* retraction-related parameters to the overall phenotype. Employing more sophisticated types of data analysis provides tools for potentially extracting such information. We therefore applied principal component analysis (PCA), which reduces multi-dimensional data sets to two hybrid parameters with specific characteristics - principal component 1 (PC1) and principal component 2 (PC2) - using the data obtained from our morphodynamic analyses for Lpd knockout and B16-F1 control cells (Fig. 4). Static parameters such as those related to geometry/curvature were excluded in this case, allowing us to investigate features that relate to cell edge dynamics. Eleven parameters were found to have the highest contribution to PC1, the majority of which

define fluctuation- or retraction-related characteristics of the cell edge (Fig. 4A). In contrast, the majority of parameters with the highest contribution to PC2 were those associated with protrusion-related characteristics of the cell edge (Fig. 4B). Thus, PC2 can be considered to define "protrusion activity", while PC1 "retraction activity". PC1 and PC2 contain 88% of the total variance of the data set. When displayed in a 2D-coordinate system, results revealed that high PC1 values (abscissa) almost entirely include cells of the Lpd knockout population, suggesting higher retraction activity upon loss of Lpd. In contrast, the majority of B16-F1 control cells display low or even negative values for PC1, indicating much lower retraction activity. In contrast, both B16-F1 wildtype and Lpd knockout cells seem to be equally spread throughout the PC2-axis, indicating higher heterogeneity in protrusion features within both populations. Together with the individual assessment of morphodynamic parameters described above, these results suggest that the major phenotype upon deletion of Lpd is related to enhanced retraction characteristics. By considering the distribution of individual cells on the PC1/PC2 2D-coordinate system, two regimes of lamellipodial protrusion are apparent. The first regime, containing a mixture of Lpd knockout cells and the majority of cells in the B16-F1 control population, was characterized with negative correlation between PC1 and PC2, indicating that cells of higher protrusion activity display lower retraction activity. Interestingly, a second regime of lamellipodial protrusion, including the majority of the Lpd knockout population, was characterized by a positive correlation between PC2 and PC1. This implies that cells with greater retraction activity also have higher protrusion activity. In order to further investigate this counterintuitive behaviour of lamellipodial dynamics, we examined the correlation between values of *Maximal Velocity during Protrusion* (parameter #6) and *Maximal Velocity during Retraction* (parameter #11), irrespective of cell genotype, but with considering and separately displaying each of the three lamellipodial protrusion patterns, smooth, intermediate and chaotic (Fig. S3A-D). We found that a positive correlation exists between these two parameters, with cells of the chaotic phenotype displaying both the highest velocity

during protrusion and the highest velocity during retraction. Only with cells of smooth phenotype, most of which harbour Lpd, we failed to detect a statistically significant correlation between protrusion and retraction velocities (Figs. 2, S3A-D). Together, these data show that loss of Lpd can bias stronger and more frequently occurring changes in the direction of cell edge movements, coinciding with compromised lamellipodial stability.

Lpd knockout does not alter the lamellipodial actin network

Our analysis reveals that Lpd deletion reduces net lamellipodial protrusion, associated with reduced persistency of protrusion caused by enhanced retraction and oscillation events. Given this, we investigated whether loss of Lpd results in general morphological or dynamic defects in lamellipodial actin networks. To our surprise, there were no obvious morphological defects or significant differences in intensity or width of lamellipodial actin in Lpd knockout cells, as compared to B16-F1 wildtype cells (Fig. 5A, B). Furthermore, loss of Lpd does not impact on the rate of actin network polymerisation and the intensity of Arp2/3 complex in lamellipodia (Fig. S3E-H). These observations indicate that reduced lamellipodial protrusion and cell migration rates upon deletion of Lpd are not caused by defects in lamellipodial actin network formation and Arp2/3 complex incorporation.

Lpd stabilizes VASP, but does not recruit VASP or Abi to lamellipodia

Lpd has previously been implicated in the recruitment and/or stabilization of Ena/VASP proteins at the lamellipodium edge or their tethering to growing actin filaments (Bae et al., 2010; Hansen and Mullins, 2015; Krause and Gautreau, 2014; Krause et al., 2004; Pula and Krause, 2008). We thus speculated that potential alterations in VASP dynamics and/or regulation might be responsible for the defects in protrusion caused by the loss of Lpd. However, there was no discernible difference in VASP localization or intensity at the very front of lamellipodia between Lpd knockout and B16-F1 wildtype cells (Fig. 6A, B). Similar results

were obtained for Mena (Fig. S3I, J). These results show that VASP and Mena accumulation at lamellipodial edges can occur in the absence of Lpd. However, immunofluoresence analysis on fixed cells does not address whether Lpd affects the kinetics of VASP in the lamellipodium. Using FRAP-based approaches, we found that the half-time of recovery of VASP is reduced in the absence of Lpd as compared to B16-F1 controls (Fig. 6C, D), whereas recovery in each case plateaus at comparable level. These data suggests that Lpd contributes to the stabilization of Ena/VASP proteins at lamellipodial edges, in spite of being dispensable for their recruitment.

Lpd is thought to promote cell migration via its interaction with the WAVE Regulatory Complex (WRC) during lamellipodium protrusion (Law et al., 2013). Immunofluorescence analysis of the WRC subunit Abl interacting protein (Abi) reveals that WRC accumulation at lamellipodia edges in the absence of Lpd is increased rather than decreased compared to control B16-F1 cells (Fig. S4A, B). However, EGFP-Abi (WRC) dynamics at the leading edge was identical in both cell types (supplementary Fig. S4C, D). This suggests that the presence of Lpd counteracts WRC recruitment to the lamellipodium edge by a hitherto unknown mechanism. Immunoblotting confirmed there were no changes in expression levels of VASP as well as the WRC subunits Abi, Nap1 and WAVE2 in Lpd knockout clones compared to B16-F1 wildtype (Figs. S4E-H). These results exclude that the relative modesty of phenotypes can be explained by compensatory changes in expression levels of respective components.

Lpd loss reduces nascent adhesion formation below lamellipodia

Since cells lacking Lpd are characterized by fluctuating and rapidly retracting lamellipodia, we hypothesized that lack of stability of these structures might be caused by defects in their adhesion to the substratum. In order to test this hypothesis, we expressed EGFP-paxillin in Lpd knockout and B16-F1 control cells, and performed live cell imaging to quantify the number of nascent adhesions during lamellipodia formation (Fig. 7A). We distinguished between front

and back halves of the lamellipodium and found that nascent adhesion distributions strongly depended on respective lamellipodial protrusion class in both cell types (Fig. 7B Movie 4). Taking all protrusion classes together, there was a clear reduction in the number of new adhesions in the absence of Lpd (Fig. 7C, left panel). Subcategorization showed that the number of new adhesions was not significantly reduced in the absence of Lpd in cells with smooth or chaotic protrusions (Fig, 7C, right panel). In contrast, the intermediate class of protrusions had a statistically significant reduction in adhesion number if Lpd was absent. This combined with the fact that the chaotic phenotype (with much lower adhesion numbers) increased in frequency in Lpd KO cells (Fig. 2C) explains the overall reduction of new adhesions in the absence of Lpd (Fig. 7C).

Although cells expressing EGFP-paxillin displayed an increase of the smooth, i.e. most efficiently protruding phenotype at the apparent expense of the intermediate phenotype in both genotypes (Fig. 7B, compare with 2D), our analysis suggests that Lpd deficiency reduces the average probability of nascent adhesions to be formed below newly protruding lamellipodia.

A closer look at the spatial distribution of adhesion formation reveals approximately a third of new adhesions form at the front part of smoothly protruding lamellipodia (Fig. 7C and Movie 4). This is consistent with new adhesions being continuously formed close to the front, with a subset being stabilized and maturing into focal adhesions, as the lamellipodium persistently moves forward. In contrast, despite having a higher total number of adhesions, cells with intermediate protrusions have significantly lower ratio of adhesion numbers in front over back parts of the lamellipodium (Fig. 7C). Moreover, adhesions appeared to accumulate at the lamellipodium-lamella border, with lower numbers of new adhesions at the front. Finally, cells with chaotic lamellipodial phenotype had very low numbers of nascent adhesions compared to the other two classes, which probably accounts for their lack of stability and frequent cycles of protrusion and retraction/collapse.

We thus conclude that Lpd helps stabilize and/or maintain nascent adhesions, which must occur indirectly since Lpd does not apparently localize to these adhesions (Fig. S1C, Movie 5). Consistently, Lpd loss also strongly shifted the balance between nascent and mature adhesions towards the latter, as Lpd-KOs display an increased area of more mature adhesions containing zyxin (Fig. 8A, B). This shift may explain the reduced efficiency of early, integrin-dependent cell spreading, in particular observed on fibronectin, but also, albeit less prominently, on laminin (Fig. S4I, J). Taken together, our data establish that loss of Lpd leads to defects in nascent adhesion formation accompanied by their increased maturation, likely contributing to the destabilization of lamellipodial protrusions.

Lpd regulates the number but not speed of Vaccinia-induced actin tails

Vaccinia virus promotes its actin-dependent cell-to-cell spread at the plasma membrane by activating the Arp2/3 complex in a Nck, WIP and N-WASP dependent fashion (Frischknecht et al., 1999b; Moreau et al., 2000; Welch and Way, 2013). Curiously, this pathway has also been linked to Rac signalling, in this case through its downstream effector FHOD1 (Alvarez and Agaisse, 2013). As Vaccinia motility and lamellipodium protrusion share features of actin-based motility, such as dependence on Arp2/3 complex activation at the plasma membrane as well as recruitment of Lpd (Krause et al., 2004) and VASP (Frischknecht et al., 1999a; Grosse et al., 2003), we investigated whether Lpd depletion affects motility of the virus. B16-F1 melanoma cells are a good model system for lamellipodia-based migration, but sensitive and unsuitable for infections. Consistent with previous immunofluorescence analysis (Krause et al., 2004), we first confirmed that both EGFP-tagged and endogenous Lpd are recruited to Vaccinia-induced actin tails in HeLa cells (Fig. S5A). RNAi-mediated knockdown of Lpd in these cells reduced the number of actin tails induced by Vaccinia relative to the control shRNA group (Fig. 9A, B). However, the length of actin tails and speed of viral movement remained unchanged upon Lpd knockdown (Fig. 9B). The observed effects were specific for actin tail

formation after viral fusion with plasma membrane, as their reduced number occurred even though there were equal numbers of extracellular virus on the plasma membrane (supplementary material, Fig. S5C). To confirm these results in an independent cell type, we employed MEFs derived from conditional Lpd (Lpd fl/fl) knockout mice (Law et al., 2013). Upon tamoxifen-induced Lpd depletion, again reduced numbers of Vaccinia actin tails per cell were observed, but as opposed to shRNA-mediated knockdown in Hela cells, the lengths of these actin tails were also reduced (Fig. 7C, D). As direct readout of actin assembly below the virus, we also assessed the speed of virus movement. However, viral speeds were unaltered in Lpd-depleted MEFs (Fig. 9D), consistent with our observations on the actin assembly rate in lamellipodia (Fig. S3E, F), Accordingly, Nck and N-WASP, which are required to activate the Arp2/3 complex as well as the prominent actin assembly regulator VASP were still recruited to the virus upon Lpd-depletion (Fig. S5D).

Taken together, our experiments suggest that Lpd can contribute to formation and maintenance of specific actin structures such as lamellipodia and Vaccinia-induced actin tails, but abrogation of Lpd expression does not eliminate these structures nor affect the efficiency of actin filament assembly in them.

DISCUSSION

Here, we explored the mechanistic function of lamellipodin (Lpd) in migrating B16-F1 cells using CRISPR/Cas9-mediated gene disruption. In agreement with previous, RNAi-mediated knockdown (Krause et al., 2004), our data confirm that Lpd is a positive regulator of lamellipodial protrusion and consequently cell migration on 2D substrates (Figure 1D, F). However, it is not obligatory for lamellipodia formation in all cell types and conditions, consistent, for instance, with reduction but not loss of lamellipodia formation upon Lpd knockdown in MTLn3 breast cancer cells (Carmona et al., 2016). This view is also compatible with Lpd knockout mice making it through embryonic development and being born, with many of them (but not all dependent on genetic background) dying early after birth (Law et al., 2013). Whatever the case, this contrasts the situation in mice lacking crucial lamellipodial regulators, such as WRC subunits (Rakeman and Anderson, 2006; Yamazaki et al., 2003) or Rac1 (Sugihara et al., 1998).

The approach of growing permanently deleted cell lines also allows exploring precise, mechanistic changes in lamellipodia formation accompanied by Lpd loss of function. Migration of B16-F1 melanoma cells on laminin is characterized by distinct protrusion phenotypes, varying from “smooth” to “chaotic” as two extremes as well as an “intermediate” phenotype, the relative frequencies of which change upon Lpd knockout (Fig. 2 and Movie 1). By means of semi-automated cell edge tracking combined with quantitative, morphodynamic analysis, we found that defects in lamellipodial persistence in Lpd knockout cells are associated with an increase in the retraction and oscillation features of their cell edge (Figs. 3 and S4). Interestingly, however, Lpd knockout cells are capable of reaching lamellipodial protrusion velocities similar to those of wildtype cells. These observations agree with the lack of detectable lamellipodial actin network defects, including F-actin densities, lamellipodial widths and actin polymerisation rates (Figs. 5 and S3E, F). All these parameters were previously found to be affected upon stable genetic removal of the lamellipodial formins FMNL2 and -3 (Kage et al.,

2017) or reduced activity of WRC (Dolati et al., 2018), so appear more sensitive to latter treatments than to the removal of Lpd. Since Lpd-KO cells did also not display any changes in lamellipodial Arp2/3 complex incorporation (Fig. S3G, H) and increased rather than decreased accumulation of its interaction partner, theWRC subunit Abi-1 (Fig. S4A, B), it is dispensable for WRC accumulation and WRC-mediated Arp2/3 complex activation, at least in B16-F1 melanoma. These data suggest that the physical interaction between Lpd and Abi has regulatory functions alternative to WRC recruitment or accumulation, the precise nature of which remain to be determined.

More surprising even, Lpd was also not essential for lamellipodial accumulation of Ena/VASP family members, but its absence increased VASP turnover at the lamellipodial edge (Fig. 6C, D). This indicates that Lpd can increase the dwell time of Ena/VASP family members at the lamellipodium edge, which may also affect the activity of the latter on growing actin filaments, as suggested by previous work (Hansen and Mullins, 2015). However, such changes are apparently too subtle to be detected in the context of the complexity of the multitude of factors potentially regulating lamellipodial actin polymerization and protrusion. Nevertheless, the absence of major phenotypes on the core actin polymerization machinery has also been recapitulated by assessing an entirely different type of plasma membrane protrusion, which is the generation of actin tails by Vaccinia virus. Although we did find a reduction in actin tail formation efficiency at the plasma membrane, which was confirmed to be independent of viral transport to the cell periphery (equal numbers of extracellular virus upon interference with Lpd function), those tails formed were not reduced in speed and recruitment features of their core actin polymerization machineries, including N-WASP and Nck, in the absence of Lpd (Figs. 9 and S5. Thus, we conclude that reduction in actin tail formation efficiencies will likely derive from mechanisms distinct from nucleating or elongating these tails, but instead from maintaining or stabilizing them within cortical actin structures, in analogy perhaps to the

phenotypes on lamellipodia maintenance described below. Specifically, lamellipodia had problems with efficiently advancing forward, at least on average, and did more likely retract, overall causing an increased Retraction to Protrusion Ratio as compared to wildtype cells (see parameter #12 in Figs. 3 and S2). Thus, increased tendency to be retracted into the cortex might also be the cause for reduced Vaccinia tail numbers, if indeed analogous.

At least when protruding on flat surfaces, lamellipodial phenotypes also correlated with, but will likely not be restricted to specific defects in adhesion dynamics. We observed total numbers of nascent adhesions in lamellipodia of Lpd knockout cells to be, on average, reduced relative to those in B16-F1 controls (Fig. 7). Conversely, numbers of mature focal adhesions, as exemplified by the presence of zyxin, were clearly increased in all Lpd knockout clones (Fig. 8). These data suggest a shift in activities from protrusive, Rac-dependent behaviour towards more contractile, Rho-dependent activity in the absence of Lpd. However, apparent defects in adhesion regulation may be linked to the various interactions of Lpd with established adhesion components such as talin or integrins (Lagarrigue et al., 2015; Lee et al., 2009; Watanabe et al., 2008). Alternatively or in addition, adhesion phenotypes may derive from defective transduction of mechanical features of extracellular matrices onto intracellular signalling complexes comprising FAK, Cas and Rac (Bae et al., 2014), but mechanistic details remain to be determined. Establishing those may not be trivial given that Lpd is restricted to the edges of protruding lamellipodia (see Movie 5) and fails to accumulate in nascent or mature adhesions. We therefore propose that Lpd loss of function causes defects in lamellipodia stability and efficiency of nascent adhesion formation by indirect, perhaps signalling-dependent mechanisms, which increase probabilities for retraction and rearward-folding of lamellipodia.

Repeated cycles of protrusion and retraction have been reported for a variety of cell types and with a broad range of periods and amplitudes (Burnette et al., 2011; Enculescu et al., 2010; Gholami et al., 2008; Giannone et al., 2004; Giannone et al., 2007; Koestler et al., 2008;

Machacek and Danuser, 2006; Zimmermann and Falcke, 2014). The chaotic behaviour that we see with increased frequencies in Lpd-KOs shows similarities to protrusion-retraction cycles in spreading fibroblasts exhibiting so called periodic contractions, which coincide with brief interruptions of protrusion and are accompanied by formation of integrin and adhesion clusters close to the cell edge (Giannone et al., 2004; Giannone et al., 2007). Although protrusion and retraction events seem less clearly separated in B16-F1 lamellipodia protruding on laminin (Fig. 1C), the loss of Lpd may well interfere with the coordination of these activities, as the likelihood of smooth, coordinated protrusion (Fig. 1C and Fig. 2) and the probability of properly coordinated nascent adhesion formation below lamellipodia (Fig. 7) are clearly compromised in the absence of Lpd. The precise changes observed upon Lpd removal concern multiple parameters (Fig. 3), which either reflect decreased protrusion and increased retraction or cell edge activities to become less predictable (parameter #16), less robust and plastic (parameters #17-20), and thus overall more chaotic. The combination of all these phenotypic parameters reduces the efficiency of protrusion and nascent adhesion formation and turnover for productive forward advancement of the lamellipodium, and ultimately the efficiency of cell migration (Fig. 1E-G). While confirming this particular aspect of previously published literature and at the same specifying the phenotypic changes caused by Lpd removal, the precise mechanistic reasons for these changes remain to be elucidated.

MATERIALS AND METHODS

Cell culture, transfection conditions, RNAi and induced Lpd knockout

B16-F1 mouse melanoma cells (purchased from American Type Culture Collection, Manassas, VA) were cultivated according to standard tissue culture conditions. Cells were grown at 37°C/7%CO_2 in DMEM medium containing 4.5g/l glucose (Life Technologies, Thermo Fisher Scientific, Germany) and 10% fetal calf serum (FCS, PAA Laboratories, Linz, Austria), 2 mM glutamine (Life Technologies), and 1% penicillin-streptomycin (Life Technologies). For transfections of B16-F1 cells with DNA vectors described below, JetPei transfection reagent (Polyplus Transfection, Illkirch, France) was used according to manufacturer's instructions. For microscopy experiments, B16-F1 cells were plated onto glass coverslips pre-coated for 1 hour at room temperature with 25 µg/ml laminin (L-2020; Sigma-Aldrich) in 50 mM Tris, pH 7.4, and 150 mM NaCl or 25 µg/ml fibronectin (Roche) in PBS.

NIH-3T3 mouse fibroblasts were grown at 37°C/7% CO_2 in DMEM medium containing 4.5g/l glucose and 10% FBS (054M3396, Sigma-Aldrich, Germany), 2mM glutamine, 1mM sodium pyruvate (Life Technologies), 1% non-essential amino acids (Life Technologies) and 1% penicillin-streptomycin.

Hela cells were maintained in DMEM supplemented with 10% FBS and antibiotics (P/S). To perform shRNA-mediated knock-down, HeLa cells were transfected with Lpd-specific or scramble shRNA as control using Fugene HD (Roche) transfection reagent, as described (Carmona et al., 2016). Following transfections, cells were incubated for 24 hours before undergoing 48-72 hours of selection with 2ug/ml puromycin, and then subjected to viral infections and analyses as described below.

Tamoxifen (4-OHT)-inducible mouse embryonic fibroblasts (Lpd fl/fl-CreER MEFs) from conditional Lpd-KO mice were generated and grown as described (Law et al., 2013). To prepare KO MEFs prior to infections, Lpd fl/fl-CreER MEFs were incubated in medium

containing 0.6µM Tamoxifen (Sigma) for 2 days, followed by 6 days incubation with 0.3uM Tamoxifen.

Generation of B16-F1 Lpd knockout cell lines

Generation of B16-F1 Lpd knockout clones was performed analogous to FMNL2/3-KO clones described previously (Kage et al., 2017). CRISPR/Cas9 guide design was performed using a publicly available CRISPR design tool (back then http://crispr.mit.edu), with the DNA sequence of exon 5 of Lamellipodin/Raph1 being used (base pairs 937-1014 of cDNA of NM_001045513.3). A guide with the highest available aggregate score of 75/100 was selected, targeting the following genomic DNA sequence: 5'-TGAGAAGATCCGAGTTGCTC-3'. Forward and reverse guide oligo sequences, respectively 5'-CACCGTGAGAAGATCCGAGTTGCTC-3' and 5'-AAACGAGCAACTCGGATCTTCTCAC-3' were annealed for 4 min at 95°C, followed by 10 min incubation at 70°C and gradual cooling at room temperature in a buffer containing 100 mM KAc, 2 mM MgAc, 30 mM HEPES-KOH (ph=4.7). Annealed sequences were cloned into an expression vector pSpCas9(BB)-2A-Puro(px459) (Addgene plasmid ID:48138) using BbsI restriction enzyme. Successful cloning was confirmed by sequencing with primer 5'-AGGCTGTTAGAGAGATAATTGG-3'. For generation of Lpd knockout cell clones, B16-F1 cells were transfected with the cloned plasmid encoding puromycin resistance and the CRISPR guide sequence targeting Lpd. Transfected cells were cultured for 4 days with B16-F1 culture medium containing 2.5 mg/ml puromycin. Single colonies were isolated and expanded until confluent. Confirmation of genetic knockout was validated by both western blot and DNA sequencing of genomic DNA. For gDNA extraction, B16-F1 cells were pelleted and incubated at 55°C overnight in lysis buffer (100 mM Tris pH 8.5, 5 mM EDTA, 0.2% SDS, 200 mM NaCl) containing 40µg/ml proteinase K. Standard phenol/chloroform precipitation was performed for extraction of nucleic acids. Genomic DNA sequence of

364bp, flanking the Lpd target sequence, was amplified by Phusion High-Fidelity Polymerase (New England Biolabs) with 5'-GAACGGGCCATTTTAAAATTGTGC-3' and 5'-AGACATTAGGAAGAATACAGTTTTACC-3' as forward and reverse primers, respectively. Amplified sequence was purified with NucleoSpin Gel and PCR clean-up kit according to the manufacturer's instructions (Macherey&Nagel), cloned into a Zero Blunt TOPO vector using Zero Blunt TOPO Cloning Kit (Invitrogen) and transformed into competent bacteria. Single bacterial colonies were isolated and inoculated, plasmid DNA purified using NucleoSpin Plasmid kit (Macherey&Nagel) and sequenced by MWG-Biotech (Ebersberg, Germany) using sequencing primer 5'-CAGGAAACAGCTATGAC-3'. Clones with frameshift mutations on all alleles causing stop codons downstream of the target site were selected for further characterization.

Live-cell imaging equipment and conditions

All live-imaging experiments were performed with either inverted Axio Observer (Carl Zeiss, Jena, Germany) equipped with an automated stage, a DG4 light source (Sutter Instrument, Novato, CA) for epifluorescence illumination, a VIS-LED for phase contrast imaging, an acousto-optic tunable filter (AOTF)-controlled 405nm diode laser for FRAP and a CoolSnap-HQ2 camera (Photometrics, Tucson, AZ), driven by VisiView software (Visitron Systems, Puchheim, Germany) or an inverted microscope (Axiovert 100 TV; Carl Zeiss), equipped with an HXP 120 lamp for epifluorescence illumination, a halogen lamp for phase-contrast imaging, a CoolSnap-HQ2 camera and electronic shutters driven by MetaMorph software (Molecular Devices, Sunnyvale, CA) for image acquisition. Cells, seeded on cover glasses, were mounted on an open heating chamber (Warner instruments, Hemden, CT) linked to a heating controller (TC-324 B) maintaining a constant temperature of 37°C. During live-imaging experiments, B16-F1 cells were incubated in microscopy medium (Ham's F-12 4-(2-hydroxyethyl)-1-piperazineethanesulfonic acid–buffered medium; Sigma-Aldrich) including

10% FCS (PAA Laboratories), 2 mM glutamine, and 1% penicillin-streptomycin (both purchased from Life Technologies).

Lamellipodium protrusion rate measurements by kymograph-based analysis

Manual determination of average lamellipodium protrusion rate was performed as previously described (Dimchev et al., 2017). Kymographs were obtained using Metamorph from time-lapse phase contrast movies of either B16-F1 wildtype cells, of Lpd knockout clones or of both overexpressing EGFP-tagged Lpd. Experiments were performed with either 63x/1.4 NA apochromatic or 100x/1.4 NA Plan apochromatic oil objectives. Average values of lamellipodial protrusion rates were displayed as μm/min.

Random migration assays

Random migration rates of B16-F1 wild type and Lpd knockout cells, seeded on 25 μg/ml laminin pre-coated μ-slide four-well glass bottom microscopy chambers (Ibidi GmbH, Martinsried, Germany), were determined using phase-contrast time-lapse movies taken with a 10x/0.15NA Plan Neofluar objective over a period of 10hrs, and time interval of 10min. Microscopy chambers were mounted on a stage equipped with an incubator maintaining a constant temperature of 37°C and 7% CO_2. Analysis was performed on ImageJ using the Manual tracking plugin and Chemotaxis and Migration Tool by Ibidi. Average values of random migration rates were displayed as μm/min.

DNA constructs

EGFP-actin and EGFP-CAAX (pEGFP-F, farnesylated) was purchased from Clontech (Mountain View, USA), and remaining constructs published previously as follows: EGFP-Lpd (Krause et al., 2004), EGFP-Abi1 (Innocenti et al., 2005), EGFP-tagged VASP and

paxillin (Rottner et al., 2001), and the Prel/RIAM expression construct, termed mmPrel1-CMV-Sport6 (Jenzora et al., 2005).

Immunoblotting and antibodies

For confirmation of CRISPR/Cas9-mediated gene disruption by Immunoblotting, protein lysates were prepared in a buffer containing 50 mM Tris (pH 7.5), 150 mM NaCl, 1 mM EDTA, 1% Triton X-100, supplemented with a Complete mini EDTA-free Protease Inhibitor Cocktail pill (Roche). For obtaining total protein lysates, cells were lysed in Laemmli sample buffer (60 mM Tris-Cl pH 6.8, 2% SDS, 10% glycerol, 5% β-mercaptoethanol, 0.01% bromophenol blue), syringed multiple times and incubated for 20 min with Benzonase nuclease (0.5µl per volume of 30µl) at 37°C in order to reduce solution viscosity caused by genomic DNA. Protein concentrations were quantified using the Pierce BCA Protein Assay Kit (Thermo Fisher Scientific). All lysates were brought to a final amount of 30µg, and boiled for 10 min at 95°C before being loaded on SDS-PAGE gels. Blotting was performed according to standard procedures using primary antibodies as follows: Two Lpd-specific antibodies were purchased from Sigma (HPA016744 recognising the N-terminus, Sigma-Aldrich, Germany) and Santa Cruz Biotechnology (European Support, Heidelberg, Germany; E-12 antibody, epitope unknown). A third Lpd antibody raised against the C-terminus of the protein was as described (Krause et al., 2004). GAPDH antibody (clone #6C5) was purchased from Calbiochem (Merck-Millipore, Germany), beta-actin antibody (ab8227) from Abcam, Germany, and Profilin1 antibody (P7624) from Sigma-Aldrich, Germany. Remaining primary antibodies were as previously published: Polyclonal VASP and PREL1 antisera (Jenzora et al., 2005), and Nap1-B (#4953-B) antiserum (Steffen et al., 2004); WAVE2 (Innocenti et al., 2004) and Abi-1/E3b1 (Biesova et al., 1997) antisera were kindly provided by Dr. Giorgio Scita (IFOM Milan, Italy). Peroxidase-coupled anti-mouse IgG or anti-rabbit IgG secondary antibodies were purchased from Dianova GmbH (Germany).

Phalloidin stainings and immunolabellings

For phalloidin stainings, cells were fixed for 20min with a mixture of pre-warmed (37°C) 4% PFA and 0.25% glutaraldehyde, followed by permeabilization in 0.1% Triton-X100/PBS for 1 min. For immunostainings of endogenous proteins, the same procedure was employed except that cells were fixed with 4% PFA alone, and for zyxin stainings, cells were permeabilized first using 0.3% Triton-X100 in 4% PFA/PBS for 1 min followed by fixation for 20 min with 4% PFA/PBS. In case of antibody stainings, samples were blocked with 5% horse serum in 1% BSA/PBS for 30-60 min. ATTO-488- and ATTO-594-labelled phalloidin were purchased from ATTO-TEC GmbH (Germany). The following primary antibodies were used: Mena monoclonal antibody A351F7D9 (Lebrand et al., 2004), monoclonal Abi antibody (clone W8.3), kindly provided by Dr. Giorgio Scita (IFOM Milan, Italy), monoclonal p16A/ArpC5A 323H3 (Olazabal et al., 2002) and monoclonal zyxin antibodies (Rottner et al., 2001). Polyclonal antibodies against murine full-length VASP (residues 1-375) were raised by immunizing a female New Zealand White rabbit with recombinant protein following 5 boosts at two-week intervals by standard procedures.

Lamellipodial width, actin filament and protein intensity measurements

Lamellipodial F-actin intensity was determined by measuring the average pixel intensities of lamellipodial regions of phalloidin-stained cells, microspikes excluded, with intensities of background regions being subtracted from lamellipodial actin intensity values. Quantitation of Arp2/3 complex intensities (p16A subunit) in the lamellipodia of different cell lines was done as described (Dimchev et al., 2017). For determining lamellipodial intensities of VASP and Abi, intensity scans from 3 pixel-wide lines drawn across lamellipodia at 3 random cellular locations were generated using Metamorph. Upon subtraction of the minimum intensity of each scan defined as background outside the cell, peak intensities from the three individual

measurements were averaged and expressed as maximum intensity counts per pixel. Lamellipodial width was quantified with Metamorph using images of phalloidin-stained cells, by drawing lines from lamellipodia tips into more proximal cellular regions up to distal edges of the lamella, followed by measuring their lengths. For each cell, lamellipodial widths in 3 random cellular locations were measured, and values averaged in order to derive the respective single value per cell; obtained values were expressed as μm.

Fluorescent recovery after photobleaching (FRAP) for investigating protein turnover or actin network polymerization rates

FRAP experiments were performed on an Axio Observer (Carl Zeiss, Jena) using a 100x/1.4NA Plan-Apochromat oil immersion objective. EGFP–VASP and –Abi, localizing at the tip of lamellipodial regions, were bleached by employing the 2D-VisiFRAP Realtime Scanner (Visitron Systems) using 60mW output power of a 405nm diode laser (Visitron Systems), in order to achieve nearly complete bleaching for each component at the lamellipodial tip. A time interval of 1500 msec and an exposure time of 500 msec were used for image acquisition. All intensity values were derived by region measurements using Metamorph software. Lamellipodial intensities before and after the bleach were corrected for background and acquisition photobleaching using regions outside of and inside the cell, respectively, and processed using Microsoft Excel. Data were fitted in SigmaPlot 12.0 (Scientific Solutions SA, Pully-Lausanne, Switzerland) using dynamic curve fits for exponential rise to maximum, and half-times of recovery calculated using equation $t_{1/2}$=-1/b*ln(0.5), as described (Dimchev and Rottner, 2018; Steffen et al., 2013).

Lamellipodial **a**ctin polymerisation rates in B16-F1 wildtype and Lpd knockout cells were obtained by photobleaching incorporated, EGFP-tagged actin. A region exceeding the lamellipodial area was bleached in each case. This allowed monitoring the recovery of fluorescence in the entire actin network over time, essentially as described previously

(Dimchev and Rottner, 2018; Kage et al., 2017; Steffen et al., 2013). Final actin network assembly rates were expressed as µm/min.

Cell spreading quantification of adhesion area

Cells were seeded onto coverslips pre-coated with either 25µg/ml laminin or 25µg/ml fibronectin (as described above). 15 min, 60 min or 3 hrs following cell seeding, coverslips were fixed with 4% PFA/0.25% glutaraldehyde, permeabilised with 0.1% Triton-X100/PBS for 1 min and stained for F-actin with phalloidin (as described above). Images were taken with 40x/1.3NA Apochromat oil objective. Cell area measurements were derived from drawing cell contours encompassing the full cell area with ImageJ, following calibration to respective objective magnification. Final data were averaged for all cells measured and displayed in μm^2.

Quantification of adhesion area in cells stained for zyxin was performed using ImageJ by manually adjusting appropriate thresholds and employing the particle analysis plugin. For enhancing accuracy, the area around the nuclear region, characterised with nonspecific background fluorescence, was excluded from measurements. Since it was challenging to separate individual adhesions in computer-aided analyses, we presented data as average, adhesion-occupied areas in percent of whole cell area.

Nascent adhesion quantification

Cells were transfected with EGFP-paxillin, and dual-channel time lapse movies (EGFP fluorescence and phase contrast) acquired on an Axio observer microscope (Carl Zeiss, see above) with 100x/1.3NA Neofluar oil immersion objective and 20 sec time interval between frames. Time-lapse movies were opened in Metamorph and brightness and contrast adjusted to optimize visualisation of lamellipodia and nascent adhesions. Lamellipodia width could be determined in both fluorescence and phase-contrast channels, due to these structures

appearing as slightly brighter and darker in respective channels, which was due to the increased concentration of actin filaments in this region. Contours encompassing the entire width of the lamellipodial regions were manually drawn on Metamorph for each time frame measured, and further separated into back and front lamellipodial regions. This was implemented by drawing multiple perpendicular lines connecting front and back of the lamellipodial region at multiple locations, and marking the middle of each perpendicular line. By connecting the middle parts of all perpendicular lines with the Metamorph multi-line tool then allowed separating the lamellipodium into two essentially equal halves. Nascent adhesions in lamellipodia were manually counted in 4 consecutive frames, and individually for back and front parts of the lamellipodium. For each cell, the number of adhesions in each region measured (either front or back) were averaged for the 4 consecutive frames, thus deriving the average number of adhesions present in each region over the course of 80 seconds. Data were presented as number of nascent adhesions per $10\mu m^2$, grouped into lamellipodial phenotype categories defined above (smooth, intermediate and chaotic), and displayed separately for back and front parts of lamellipodia.

Vaccinia virus infections

Cell lines were infected with the WR strain of vaccinia virus and processed for immunofluorescence as previously described (Arakawa et al., 2007a; Arakawa et al., 2007b). In case of HeLa, the cells were fixed at 9 hr post-infection and for KO MEFs at 15 hr post-infection. The following antibodies were used for immunofluorescence: Nck (Millipore), N-WASP (Moreau et al., 2000), VASP (BD Transduction Laboratories), Lpd (Krause et al., 2004), B5 (Hiller and Weber, 1985). Actin tails were stained with Alexa Texas Red or 488 phalloidin (Invitrogen) and viral DNA was observed using DAPI staining. The quantification of number of actin tails and number of extracellular virus was performed through manual counting, all other analyses were performed as described previously (Humphries et al., 2014).

For all quantifications, counts were performed over multiple cells in three separate experiments, with the n in each case given in the figure legend. Graphs and statistics were compiled using Prism (Graphpad software, USA), comparison of two data sets was carried out using an unpaired t-test.

Cell edge tracking for lamellipodial morphodynamic analysis

Cells were transfected with EGFP-CAAX construct, and time-lapse movies acquired on an inverted microscope (Axiovert 100 TV; Carl Zeiss) using a 100x/1.4NA Plan-apochromatic oil immersion objective, with a time interval of 1 second. To enhance cell edge detection, acquired fluorescent time-lapse movies were processed on ImageJ with *Smooth, Gaussian blur*, *Enhance contrast* and *Find edges* filters. Brightness and contrast levels were further adjusted to obtain optimal separation of edge from background. Cell edge analysis was initiated with ImageJ by using the JFilament 2D plugin (Smith et al., 2010b). The following *JFilament* parameters were found optimal for B16-F1 cell edge detection with aforementioned acquisition settings: Alpha=15, Beta=10, Gamma=4000, Weight=0.3, Stretch Force=15, Deform iterations=400, Point Spacing=5, Image Smoothing=1.01. 120 frames (i.e. 2min of acquisition time) were processed in order to obtain "snake" files (or snakes), each one containing the spatiotemporal positions of the tracked cell contour, defined by x and y coordinates of a given number of points. Snake files were processed in Matlab R2017a (Mathworks, Massachusetts, United States), in order to derive velocity, curvature maps and specific morphodynamic parameters.

Matlab script and displacement field of the contour

Following cell edge tracking and obtaining contour coordinates from Jfilament for every frame, a Matlab script was employed to calculate the displacement and velocity fields, using a method aiming to determine the correspondences of points on the measured cell edge contour

over subsequent frames. The figure below illustrates the mechanical spring system employed to find the corresponding positions of points between curve in time step t (i.e. C_t), and curve in time step $t+1$ (i.e. C_{t+1}) where t is an arbitrary time frame.

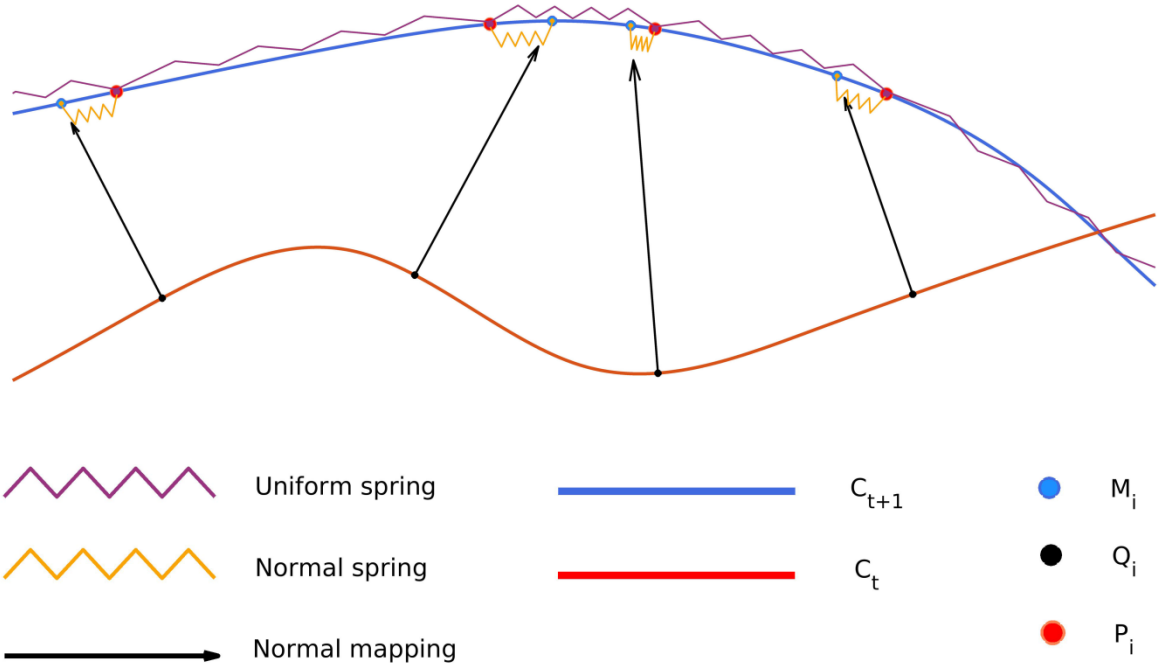

For regions where curves in two subsequent frames are parallel, the assumption is that each point is moved in the normal direction and the correspondence between curves is achieved by following the normal vectors from C_t, to C_{t+1}. For regions of high deformations and enhanced convexity or concavity in one of the curves, meaning the curves not being parallel to each other, a normal mapping would not be reliable. In these situations, uniform mapping is employed resulting in evenly spaced distribution of points on C_{t+1}. In order to add an adaptivity feature to the correspondence algorithm, normal and uniform mappings along the curves were combined, but with variable weights, the latter being defined as a function of local deformation or parallelism degree. The variability of weights enabled constructing the basis of the mapping between two curves, relying on the normal mapping method in the regions of low deformation, followed by using the uniform mapping to interpolate the mapping in the regions of high deformation. In order to implement this principle, a mechanical spring model was employed similar to the one described previously (Machacek

and Danuser, 2006), containing two types of springs: springs of normal or uniform mapping. Unlike the mechanical model used by Machacek and Danuser (2006), in our model the springs responsible for normal mapping were also considered as linear springs and all the springs are assumed to be bound to the cell boundary. This simplifies the nonlinear spring system to a linear one in the 1D arc length coordinate, and facilitates the computations.

At each time point t, there are N fixed nodes Q_i, i= 1:N on C_t , whose coordinates are obtained by applying the same procedure in the previous time frame, and the aim of the algorithm is to find the position of their corresponding nodes P_i, i= 1:N on C_{t+1}.

Nodes on C_{t+1} are connected by two kinds of springs. Uniform mapping springs connect neighbouring nodes and their rest length is defined as $l_{0\ t+1}=L_{t+1}/N$, where L_{t+1} is total length of the curve C_{t+1}.

Normal mapping springs connect each node P_i to its normally mapped position M_i, i= 1:N, which is defined as the intersection of curve C_{t+1} and normal vector from Q_i on curve C_t (see figure). The rest length of these springs is zero, thus they tend to attract nodes toward their normally mapped positions M_i. The strength of this attraction depends on the spring constant, the latter depending on deformation degree.

Degree of deformation at each node P_i was defined as:

$$D(i)= c_1 \left| (l(i)+l(i+1))/2 - l_{0\,t} \right| + c_2 \left| l(i+1) - l(i) \right| + c_3 \max\{ 0 , -(l(i)+l(i+1))/2 \}$$

Where c_1, c_2, c_3 are constants and l(i) is the length of the segment of C_{t+1} between M_{i-1} and M_i, which can be negative if M_i appears before M_{i-1}.

The first term in aforementioned equation decreases in the regions where curves C_t and C_{t+1} are close to parallelism, i.e. it measures the similarity of the direction of curves C_t and C_{t+1} at any point i. The second term captures the similarity of the curvature of curves C_t and C_{t+1} at any point i. The third term penalises the regions where the order of M points does not match the order of Q nodes. In these regions, the additional increase in deformation degree caused by the third term reduces the possibility of topological violations, which is the difference between the order of P nodes and Q nodes.

Spring constants for normal mapping springs and uniform mapping springs were defined as functions of degree of deformation:

$$K_{normal} = k_1 / (k_1 + k_2 D)$$

$$K_{uniform} = k_3 . D / (k_1 + k_2 D)$$

Where k_1, k_2 and k_3 are constants.

These relations indicate the predominance of uniform and normal mapping in, respectively, high and low deformation regions.

For each time point t, a system of N nodes on C_{t+1} was constructed, which are connected by different springs, as explained above. In order to find unknown positions of nodes P_i , N force balance equations were solved. By using the positions of nodes Q_i and their corresponding nodes P_i, the displacement and velocity fields of the curve C_t were found. The effects of curve ends on the mapping were taken into consideration. The result of the mapping, especially in the regions close to ends, can depend on the position of end points of the curves in different

time frames, and in order to compensate for this dependency, 5% of the snake lengths at both ends of tracked contours were removed.

Quantitative analysis of cell edge morphodynamic metrics and PCA analysis

Finding the corresponding location of each point on the tracked cell edge allowed deriving the trajectory of each point over time and obtaining the velocity of each point between different frames. Once the local velocities of points along the cell boundary were calculated, velocity maps were constructed by plotting velocity data in a 2D coordinate system, with time and position along the cell boundary defined as x- and y-axis, respectively. The velocity at any point on curve and any time was indicated by colours, as shown in Figure 2. For the morphodynamic behaviour of the leading edge, only the normal component of the velocity was considered. Similarly, maps for curvature along the cell boundary in time were constructed. Since the curve in our model is a piecewise linear curve represented by a finite number of points, the local curvature at any point was calculated using the position data of the point and its two neighbouring points. The velocity and curvature maps contain the majority of morphodynamical information of the analysed edge. The morphodynamical behaviour of cells was subsequently quantified by defining descriptors based on these maps (explained in Supplementary Table S1). Principal Component Analysis (PCA) was performed on the defined morphodynamical metrics, using Matlab.

Image Processing and Statistical analysis

Brightness and contrast levels were adjusted using MetaMorph software v7.7.8.0. Figures were processed and assembled on Adobe Photoshop CS4 (Adobe Systems, San Jose, CA). Data analyses were performed with MetaMorph, Fiji or ImageJ, Microsoft Excel 2010 and Sigma plot 12.0 (Systat Software, Erkrath, Germany). Data sets were compared with paired t-tests (if normally distributed) or alternatively, non-parametric Mann–Whitney rank sum tests

using Sigma plot. Probability of error of 5% or less ($*p < 0.05$) was considered as statistically significant.

ACKNOWLEDGMENTS

We would also like to thank Giorgio Scita for reagents, Naoko Kogata (The Francis Crick Institute, London, UK) for help with assembling Vaccinia-related figures, Frieda Kage (Geisel School of Medicine at Dartmouth, Hanover, NH, USA) for fruitful discussions, and Brigitte Denker for excellent technical assistance.

COMPETING INTERESTS

No competing interests declared.

FUNDING

This work was supported in part by the Deutsche Forschungsgemeinschaft (DFG), grants GRK2223/1, RO2414/5-1 (to K.R.), FA350/11-1 (to M.F.) and FA330/11-1 (to J.F.), as well as by intramural funding from the Helmholtz Society (to T.E.B.S. and K.R.). ACH and MW are supported by the Francis Crick Institute, which receives its core funding from Cancer Research UK (FC001209), the UK Medical Research Council (FC001209), and the Wellcome Trust (FC001209). MK is supported by the Biotechnology and Biological Science Research Council, UK (BB/F011431/1; BB/J000590/1; BB/N000226/1).

FIGURE LEGENDS

Fig. 1. Lamellipodin (Lpd) deletion in B16-F1 cells reduces rates of lamellipodial protrusion and random migration. (A) Immunoblot analysis using an antibody recognizing the C-terminus of Lpd demonstrates the Lpd KO#3, #8 and #10 cell lines do not contain detectable levels of the protein. GAPDH represents a loading control (B) Table summarizes the genomic DNA sequencing of the Lpd KO#3, #8 and #10 cell lines from at least 20 sequencing reactions each. (C) Kymography on protruding lamellipodia of B16-F1 wildtype and Lpd-KO cells or either cell type expressing EGFP-Lpd, as indicated over a 5 min interval. (D) Quantitation of average lamellipodial advancement rates using kymography as raw data. (E) Trajectory plots derived from manual tracking of individually migrating cells of the indicated genotypes on laminin. Colours indicate average directions (north/south) of migration paths with starting points set to (0,0). (F) Quantitation of the data shown in E. (G) Mean square displacement over time of B16-F1 control and the Lpd KO pool derived from data in E. All quantified data are displayed as arithmetic means +/- SEM, with asterisks above bar charts indicating statistically significant differences between designated groups, * = $p<0.05$, and n = number of cells analysed.

Fig. 2. Deletion of Lpd changes the balance between lamellipodial protrusion phenotypes. (A) Illustration of three distinct types of lamellipodial protrusion phenotypes in B16-F1 WT cells using computer-aided analyses of cell edge dynamics. Phenotypes are represented by the spatiotemporal evolution of measured cell edge contours, with time increasing from blue to red over 120 seconds. (B) Example velocity maps, representing smooth, intermediate and chaotic lamellipodial phenotypes, as derived by plotting the velocities of individual points into a 2D-coordinate system, with normalized distance of points along the edge on the y-axis and time on the x-axis. Retraction velocities are indicated in blue,

and protrusion velocities in red (µm/sec). (C) Example curvature maps for each protrusion phenotype, as indicated, and individually derived by plotting local curvatures of individual points into a 2D-coordinate system, with normalized distance of points along the edge on the y-axis and time on the x-axis. Concave and convex curvatures are indicated in blue and red, respectively. (D) Quantification of the fraction of cells with indicated genotypes displaying each lamellipodial phenotype (smooth, intermediate or chaotic). Lpd knockout cells represent a pool of the three knockout clones.

Fig. 3. Morphodynamic analysis of lamellipodial protrusion of B16-F1 control and Lpd knockout cells.

Parameters characterizing protrusion-, retraction-, velocity- or geometry-related characteristics of cell edge movements in B16-F1 wildtype and Lpd knockout cells, as derived from quantitative, morphodynamic analysis of lamellipodial protrusion. Data are represented as arithmetic means +/- SEM (asterisks indicate statistically significant differences, with * = $p<0.05$). In order to facilitate the visualization of relative differences in lamellipodial morphodynamics between wildtype (marked with blue line) and Lpd knockout cells (marked with red line), 20 selected morphodynamic parameters (indicated with green numbers on y-axis) were each normalized by assigning their respective means to 0 and scaling their STD values to 1. For description of each parameter, see Table S1.

Fig. 4. PCA analysis reveals distinct lamellipodial protrusion regimes for B16-F1 control *versus* Lpd knockout cells.

(A, B) Figures display the loadings contributed by the individual parameters (derived from quantitative morphodynamic analysis) to principal components 1 and 2 (A: PC1, B: PC2). The larger the absolute value of a given loading, the stronger a given parameter contributes to respective PC. Loadings of high contribution are marked in yellow/orange. The parameter

numbers correspond to those displayed in Figure 3 and Table S1, except for curvature/geometry-related parameters, which were excluded. Based on respective parameter contributions, PC1 mostly reflects retraction, and PC2 protrusion activity. (C) B16-F1 control cells (blue) and Lpd knockout cells (red) are plotted in a 2D-coordinate system with PC1 (containing 58% of total variance) and PC2 (containing 30% of total variance) on x- and y-axis, respectively. Each dot indicates a single cell, and spatiotemporal, lamellipodial contours of 8 selected cells (circles) are arranged radially around the graph, to exemplify the dynamic, lamellipodial patterns of individual, representative cells located in different sections of the PC1-PC2-plane (time-colour code as described for Fig. 2A). Cells with enhanced retraction are characterized by higher PC1 values and thus shifted towards the right of the x-axis. Cells with enhanced protrusion are characterized with higher PC2 values and shifted towards the top of the y-axis. Based on this type of data representation, two major protrusion regimes can be distinguished in our cells. Regime 1, containing most cells of the B16-F1 wild-type population and characterized by a negative correlation between PC1 and PC2 (indicated with pink line and Spearman correlation coefficient of -0.74, $p<0.001$), and regime 2, comprised mostly of cells of the Lpd knockout population and characterized by a positive correlation between PC1 and PC2 (indicated with light green line and Spearman correlation coefficient of 0.58, $p<0.001$). Dominance of a specific parameter in the characterization of the morphodynamics of a cell corresponds to a parameter-specific direction in the PC1-PC2-plane (green numbers). The morphodynamic characterization of cells positioned on a line from the origin to a specific green number is dominated by the parameter with this number.

Fig. 5. Lpd KO cells lack discernible defects in lamellipodial actin networks. (A) B16-F1 cells of indicated genotype migrating on laminin, and fixed and stained for F-actin with phalloidin. (B) Graphs show quantitation of lamellipodial F-actin intensity and lamellipodial width of individual Lpd KO clones and the pooled population compared to controls.

n=number of cells, and data are represented as arithmetic means +/- SEM. Statistics revealed no significant differences between any pair of experimental groups (not shown).

Fig. 6. Analysis of VASP intensity and turnover at lamellipodia edges in the presence and absence of Lpd.

(A) Immunofluorescent analysis showing the localization of VASP at lamellipodia edges in both B16-F1 control and Lpd knockout cells. (B) Quantification of VASP intensities at lamellipodia edges in B16-F1 wildtype and Lpd knockout cells, displayed individually and as pooled population. n = number of cells, and data are arithmetic means +/- SEM. (C) The graph shows the recovery curves of EGFP-tagged VASP at the leading edge after bleaching in B16-F1 cells and individual Lpd knockout clones, as indicated. Half-times of recovery (in seconds) obtained from curve fitting are displayed on the right. Each time point after the bleach is represented as arithmetic mean ± SEM. (D) Fluorescent recovery curve fits of lamellipodial FRAP data of B16-F1 wildtype and pooled Lpd KO cells as well as derived $t_{1/2}$-values, as indicated on the right. n = number of FRAP events analysed.

Fig. 7. Formation of nascent adhesions is compromised by deletion of Lpd.

(A) Representative, EGFP-paxillin and phase contrast images of protrusive regions of B16-F1 wild-type or Lpd knockout cells, with the front halves of their lamellipodia encircled with cyan, and the back halves with yellow. Images display distributions of nascent adhesions in the three distinct lamellipodial protrusion phenotypes defined in Figure 2. (B) Table indicating cell fractions belonging to each protrusion phenotype (smooth, intermediate or chaotic) for both control and Lpd KO cell populations upon EGFP-paxillin expression. The Lpd KO population corresponds to data from Lpd KO#3. The ratio of cells Lpd KO over B16-F1 for each protrusion phenotype is shown in the fourth column on the right, again confirming significantly reduced cell numbers among Lpd knockout cells as compared to controls

harbouring the smooth lamellipodial phenotype, and *vice versa* for the chaotic phenotype. (C) Quantification of nascent adhesion numbers in lamellipodia of each protrusion phenotype (smooth, intermediate or chaotic), as well as averaged for all phenotypes and displayed for both genotypes (B16-F1 wildtype and Lpd KO) separately (left). Quantifications are also separated for front and back lamellipodial regions, again highlighted as cyan and yellow bars, respectively. Data are arithmetic means +/- SEM, and asterisks above bar charts indicate statistically significant differences, with * = $p<0.05$.

Fig. 8. Lpd removal enhances the area occupied by focal adhesions. (A) B16-F1 wildtype or Lpd knockout clones were seeded onto laminin and mature focal adhesions stained with Zyxin-reactive antibody. Green arrows point at typical clusters of focal adhesions more frequently observed in Lpd knockout clones. (B) Quantitation of average focal adhesion area (relative to cell area) as determined in distinct cell types as indicated. All data are arithmetic means +/- SEM, with asterisks above bar charts indicating statistically significant differences between designated groups (* = $p<0.05$), n equals numbers of cells analysed.

Fig. 9. Frequency of Vaccinia actin tail formation, but not their rate of motility is reduced by Lpd depletion. (A) Representative immunofluorescence images of HeLa cells treated with control and Lpd shRNA. In both cases, phalloidin staining reveals actin tails induced by vaccinia virus. The reduction in Lpd levels by shRNA was confirmed by immunoblot. (B) Quantification of the number of actin tails per cell (n=45 cells), the length of actin tails (n=200 tails), and the speed of viral movement (n=50 viruses), in control and Lpd shRNA-treated cells. (C) Fluorescence images of actin tails (red-phalloidin) produced by vaccinia (green-DAPI) in parental and Lpd KO MEFs, as indicated. (D) Quantification of the number of actin tails per cell (n=50 cells), the length of actin tails (n=100 tails), and the speed of viral movement (n=50 viruses), in control (Lpd *fl/fl*) and Lpd KO MEFs. Red lines

correspond to arithmetic means, and error bars SEM from three independent experiments. ****P < 0.0001, **P < 0.01, n.s., not significant.

References

Alvarez, D.E., and H. Agaisse. 2013. The formin FHOD1 and the small GTPase Rac1 promote vaccinia virus actin-based motility. *J Cell Biol*. 202:1075-1090.

Arakawa, Y., J.V. Cordeiro, S. Schleich, T.P. Newsome, and M. Way. 2007a. The release of vaccinia virus from infected cells requires RhoA-mDia modulation of cortical actin. *Cell Host Microbe*. 1:227-240.

Arakawa, Y., J.V. Cordeiro, and M. Way. 2007b. F11L-mediated inhibition of RhoA-mDia signaling stimulates microtubule dynamics during vaccinia virus infection. *Cell Host Microbe*. 1:213-226.

Bachir, A.I., A.R. Horwitz, W.J. Nelson, and J.M. Bianchini. 2017. Actin-Based Adhesion Modules Mediate Cell Interactions with the Extracellular Matrix and Neighboring Cells. *Cold Spring Harb Perspect Biol*. 9.

Bae, Y.H., Z. Ding, T. Das, A. Wells, F. Gertler, and P. Roy. 2010. Profilin1 regulates PI(3,4)P2 and lamellipodin accumulation at the leading edge thus influencing motility of MDA-MB-231 cells. *Proc Natl Acad Sci U S A*. 107:21547-21552.

Bae, Y.H., K.L. Mui, B.Y. Hsu, S.L. Liu, A. Cretu, Z. Razinia, T. Xu, E. Pure, and R.K. Assoian. 2014. A FAK-Cas-Rac-lamellipodin signaling module transduces extracellular matrix stiffness into mechanosensitive cell cycling. *Sci Signal*. 7:ra57.

Biesova, Z., C. Piccoli, and W.T. Wong. 1997. Isolation and characterization of e3B1, an eps8 binding protein that regulates cell growth. *Oncogene*. 14:233-241.

Bodo, C., C. Fernandes, and M. Krause. 2017. Brain specific Lamellipodin knockout results in hyperactivity and increased anxiety of mice. *Sci Rep*. 7:5365.

Boucrot, E., A.P. Ferreira, L. Almeida-Souza, S. Debard, Y. Vallis, G. Howard, L. Bertot, N. Sauvonnet, and H.T. McMahon. 2015. Endophilin marks and controls a clathrin-independent endocytic pathway. *Nature*. 517:460-465.

Burnette, D.T., S. Manley, P. Sengupta, R. Sougrat, M.W. Davidson, B. Kachar, and J. Lippincott-Schwartz. 2011. A role for actin arcs in the leading-edge advance of migrating cells. *Nat Cell Biol*. 13:371-381.

Carmona, G., U. Perera, C. Gillett, A. Naba, A.L. Law, V.P. Sharma, J. Wang, J. Wyckoff, M. Balsamo, F. Mosis, M. De Piano, J. Monypenny, N. Woodman, R.E. McConnell, G. Mouneimne, M. Van Hemelrijck, Y. Cao, J. Condeelis, R.O. Hynes, F.B. Gertler, and M. Krause. 2016. Lamellipodin promotes invasive 3D cancer cell migration via regulated interactions with Ena/VASP and SCAR/WAVE. *Oncogene*. 35:5155-5169.

Chan Wah Hak, L., S. Khan, I. Di Meglio, A.L. Law, S. Lucken-Ardjomande Hasler, L.M. Quintaneiro, A.P.A. Ferreira, M. Krause, H.T. McMahon, and E. Boucrot. 2018. FBP17 and CIP4 recruit SHIP2 and lamellipodin to prime the plasma membrane for fast endophilin-mediated endocytosis. *Nat Cell Biol*. 20:1023-1031.

Colo, G.P., E.M. Lafuente, and J. Teixido. 2012. The MRL proteins: adapting cell adhesion, migration and growth. *Eur J Cell Biol*. 91:861-868.

Dimchev, G., and K. Rottner. 2018. Micromanipulation Techniques Allowing Analysis of Morphogenetic Dynamics and Turnover of Cytoskeletal Regulators. *J Vis Exp*.

Dimchev, G., A. Steffen, F. Kage, V. Dimchev, J. Pernier, M.F. Carlier, and K. Rottner. 2017. Efficiency of lamellipodia protrusion is determined by the extent of cytosolic actin assembly. *Mol Biol Cell*. 28:1311-1325.

Dolati, S., F. Kage, J. Mueller, M. Musken, M. Kirchner, G. Dittmar, M. Sixt, K. Rottner, and M. Falcke. 2018. On the relation between filament density, force generation, and protrusion rate in mesenchymal cell motility. *Mol Biol Cell*. 29:2674-2686.

Enculescu, M., M. Sabouri-Ghomi, G. Danuser, and M. Falcke. 2010. Modeling of protrusion phenotypes driven by the actin-membrane interaction. *Biophys J*. 98:1571-1581.

Frischknecht, F., S. Cudmore, V. Moreau, I. Reckmann, S. Rottger, and M. Way. 1999a. Tyrosine phosphorylation is required for actin-based motility of vaccinia but not Listeria or Shigella. *Curr Biol*. 9:89-92.

Frischknecht, F., V. Moreau, S. Rottger, S. Gonfloni, I. Reckmann, G. Superti-Furga, and M. Way. 1999b. Actin-based motility of vaccinia virus mimics receptor tyrosine kinase signalling. *Nature*. 401:926-929.

Gholami, A., M. Falcke, and E. Frey. 2008. Velocity oscillations in actin-based motility. *New Journal of Physics*. 10:033022.

Giannone, G., B.J. Dubin-Thaler, H.G. Dobereiner, N. Kieffer, A.R. Bresnick, and M.P. Sheetz. 2004. Periodic lamellipodial contractions correlate with rearward actin waves. *Cell*. 116:431-443.

Giannone, G., B.J. Dubin-Thaler, O. Rossier, Y. Cai, O. Chaga, G. Jiang, W. Beaver, H.G. Dobereiner, Y. Freund, G. Borisy, and M.P. Sheetz. 2007. Lamellipodial actin mechanically links myosin activity with adhesion-site formation. *Cell*. 128:561-575.

Grosse, R., J.W. Copeland, T.P. Newsome, M. Way, and R. Treisman. 2003. A role for VASP in RhoA-Diaphanous signalling to actin dynamics and SRF activity. *EMBO J*. 22:3050-3061.

Hansen, S.D., and R.D. Mullins. 2015. Lamellipodin promotes actin assembly by clustering Ena/VASP proteins and tethering them to actin filaments. *Elife*. 4.

Hiller, G., and K. Weber. 1985. Golgi-derived membranes that contain an acylated viral polypeptide are used for vaccinia virus envelopment. *J Virol*. 55:651-659.

Humphries, A.C., S.K. Donnelly, and M. Way. 2014. Cdc42 and the Rho GEF intersectin-1 collaborate with Nck to promote N-WASP-dependent actin polymerisation. *J Cell Sci*. 127:673-685.

Innocenti, M., S. Gerboth, K. Rottner, F.P. Lai, M. Hertzog, T.E. Stradal, E. Frittoli, D. Didry, S. Polo, A. Disanza, S. Benesch, P.P. Di Fiore, M.F. Carlier, and G. Scita. 2005. Abi1 regulates the activity of N-WASP and WAVE in distinct actin-based processes. *Nat Cell Biol*. 7:969-976.

Innocenti, M., A. Zucconi, A. Disanza, E. Frittoli, L.B. Areces, A. Steffen, T.E. Stradal, P.P. Di Fiore, M.F. Carlier, and G. Scita. 2004. Abi1 is essential for the formation and activation of a WAVE2 signalling complex. *Nat Cell Biol*. 6:319-327.

Jenzora, A., B. Behrendt, J.V. Small, J. Wehland, and T.E. Stradal. 2005. PREL1 provides a link from Ras signalling to the actin cytoskeleton via Ena/VASP proteins. *FEBS Lett*. 579:455-463.

Kage, F., M. Winterhoff, V. Dimchev, J. Mueller, T. Thalheim, A. Freise, S. Bruhmann, J. Kollasser, J. Block, G.A. Dimchev, M. Geyer, H.J. Schnittler, C. Brakebusch, T.E. Stradal, M.F. Carlier, M. Sixt, J. Kas, J. Faix, and K. Rottner. 2017. FMNL formins boost lamellipodial force generation. *Nat Commun*. accepted.

Koestler, S.A., S. Auinger, M. Vinzenz, K. Rottner, and J.V. Small. 2008. Differentially oriented populations of actin filaments generated in lamellipodia collaborate in pushing and pausing at the cell front. *Nat Cell Biol*. 10:306-313.

Krause, M., and A. Gautreau. 2014. Steering cell migration: lamellipodium dynamics and the regulation of directional persistence. *Nature reviews. Molecular cell biology*. 15:577-590.

Krause, M., J.D. Leslie, M. Stewart, E.M. Lafuente, F. Valderrama, R. Jagannathan, G.A. Strasser, D.A. Rubinson, H. Liu, M. Way, M.B. Yaffe, V.A. Boussiotis, and F.B. Gertler. 2004. Lamellipodin, an Ena/VASP ligand, is implicated in the regulation of lamellipodial dynamics. *Dev Cell*. 7:571-583.

Lagarrigue, F., P. Vikas Anekal, H.S. Lee, A.I. Bachir, J.N. Ablack, A.F. Horwitz, and M.H. Ginsberg. 2015. A RIAM/lamellipodin-talin-integrin complex forms the tip of sticky fingers that guide cell migration. *Nat Commun*. 6:8492.

Law, A.L., A. Vehlow, M. Kotini, L. Dodgson, D. Soong, E. Theveneau, C. Bodo, E. Taylor, C. Navarro, U. Perera, M. Michael, G.A. Dunn, D. Bennett, R. Mayor, and M. Krause. 2013. Lamellipodin and the Scar/WAVE complex cooperate to promote cell migration in vivo. *J Cell Biol*. 203:673-689.

Lebrand, C., E.W. Dent, G.A. Strasser, L.M. Lanier, M. Krause, T.M. Svitkina, G.G. Borisy, and F.B. Gertler. 2004. Critical role of Ena/VASP proteins for filopodia formation in neurons and in function downstream of netrin-1. *Neuron*. 42:37-49.

Lee, H.S., C.J. Lim, W. Puzon-McLaughlin, S.J. Shattil, and M.H. Ginsberg. 2009. RIAM activates integrins by linking talin to ras GTPase membrane-targeting sequences. *J Biol Chem*. 284:5119-5127.

Machacek, M., and G. Danuser. 2006. Morphodynamic profiling of protrusion phenotypes. *Biophys J*. 90:1439-1452.

Michael, M., A. Vehlow, C. Navarro, and M. Krause. 2010. c-Abl, Lamellipodin, and Ena/VASP proteins cooperate in dorsal ruffling of fibroblasts and axonal morphogenesis. *Curr Biol*. 20:783-791.

Moreau, V., F. Frischknecht, I. Reckmann, R. Vincentelli, G. Rabut, D. Stewart, and M. Way. 2000. A complex of N-WASP and WIP integrates signalling cascades that lead to actin polymerization. *Nat Cell Biol*. 2:441-448.

Olazabal, I.M., E. Caron, R.C. May, K. Schilling, D.A. Knecht, and L.M. Machesky. 2002. Rho-kinase and myosin-II control phagocytic cup formation during CR, but not FcgammaR, phagocytosis. *Curr Biol*. 12:1413-1418.

Omotade, O.F., S.L. Pollitt, and J.Q. Zheng. 2017. Actin-based growth cone motility and guidance. *Mol Cell Neurosci*. 84:4-10.

Pula, G., and M. Krause. 2008. Role of Ena/VASP proteins in homeostasis and disease. *Handb Exp Pharmacol*:39-65.

Rakeman, A.S., and K.V. Anderson. 2006. Axis specification and morphogenesis in the mouse embryo require Nap1, a regulator of WAVE-mediated actin branching. *Development*. 133:3075-3083.

Rottner, K., B. Behrendt, J.V. Small, and J. Wehland. 1999. VASP dynamics during lamellipodia protrusion. *Nat Cell Biol*. 1:321-322.

Rottner, K., J. Faix, S. Bogdan, S. Linder, and E. Kerkhoff. 2017. Actin assembly mechanisms at a glance. *J Cell Sci*. 130:3427-3435.

Rottner, K., M. Krause, M. Gimona, J.V. Small, and J. Wehland. 2001. Zyxin is not colocalized with vasodilator-stimulated phosphoprotein (VASP) at lamellipodial tips and exhibits different dynamics to vinculin, paxillin, and VASP in focal adhesions. *Mol Biol Cell*. 12:3103-3113.

Schaks, M., S.P. Singh, F. Kage, P. Thomason, T. Klunemann, A. Steffen, W. Blankenfeldt, T.E. Stradal, R.H. Insall, and K. Rottner. 2018. Distinct Interaction Sites of Rac GTPase with WAVE Regulatory Complex Have Non-redundant Functions in Vivo. *Curr Biol*. 28:3674-3684 e3676.

Smith, K., D. Humphreys, P.J. Hume, and V. Koronakis. 2010a. Enteropathogenic Escherichia coli recruits the cellular inositol phosphatase SHIP2 to regulate actin-pedestal formation. *Cell Host Microbe*. 7:13-24.

Smith, M.B., H. Li, T. Shen, X. Huang, E. Yusuf, and D. Vavylonis. 2010b. Segmentation and tracking of cytoskeletal filaments using open active contours. *Cytoskeleton (Hoboken)*. 67:693-705.

Steffen, A., M. Ladwein, G.A. Dimchev, A. Hein, L. Schwenkmezger, S. Arens, K.I. Ladwein, J. Margit Holleboom, F. Schur, J. Victor Small, J. Schwarz, R. Gerhard, J.

Faix, T.E. Stradal, C. Brakebusch, and K. Rottner. 2013. Rac function is crucial for cell migration but is not required for spreading and focal adhesion formation. *Journal of cell science*. 126:4572-4588.

Steffen, A., K. Rottner, J. Ehinger, M. Innocenti, G. Scita, J. Wehland, and T.E. Stradal. 2004. Sra-1 and Nap1 link Rac to actin assembly driving lamellipodia formation. *EMBO J*. 23:749-759.

Sugihara, K., N. Nakatsuji, K. Nakamura, K. Nakao, R. Hashimoto, H. Otani, H. Sakagami, H. Kondo, S. Nozawa, A. Aiba, and M. Katsuki. 1998. Rac1 is required for the formation of three germ layers during gastrulation. *Oncogene*. 17:3427-3433.

Vehlow, A., D. Soong, G. Vizcay-Barrena, C. Bodo, A.L. Law, U. Perera, and M. Krause. 2013. Endophilin, Lamellipodin, and Mena cooperate to regulate F-actin-dependent EGF-receptor endocytosis. *EMBO J*. 32:2722-2734.

Wang, C., H.J. Choi, S.J. Kim, A. Desai, N. Lee, D. Kim, Y. Bae, and K. Lee. 2018. Deconvolution of subcellular protrusion heterogeneity and the underlying actin regulator dynamics from live cell imaging. *Nat Commun*. 9:1688.

Wang, J., J.E. King, M. Goldrick, M. Lowe, F.B. Gertler, and I.S. Roberts. 2015. Lamellipodin Is Important for Cell-to-Cell Spread and Actin-Based Motility in Listeria monocytogenes. *Infect Immun*. 83:3740-3748.

Watanabe, N., L. Bodin, M. Pandey, M. Krause, S. Coughlin, V.A. Boussiotis, M.H. Ginsberg, and S.J. Shattil. 2008. Mechanisms and consequences of agonist-induced talin recruitment to platelet integrin alphaIIbbeta3. *J Cell Biol*. 181:1211-1222.

Welch, M.D., and M. Way. 2013. Arp2/3-mediated actin-based motility: a tail of pathogen abuse. *Cell host & microbe*. 14:242-255.

Yamazaki, D., S. Suetsugu, H. Miki, Y. Kataoka, S. Nishikawa, T. Fujiwara, N. Yoshida, and T. Takenawa. 2003. WAVE2 is required for directed cell migration and cardiovascular development. *Nature*. 424:452-456.

Zimmermann, J., and M. Falcke. 2014. Formation of transient lamellipodia. *PLoS One*. 9:e87638.

Fig. 1

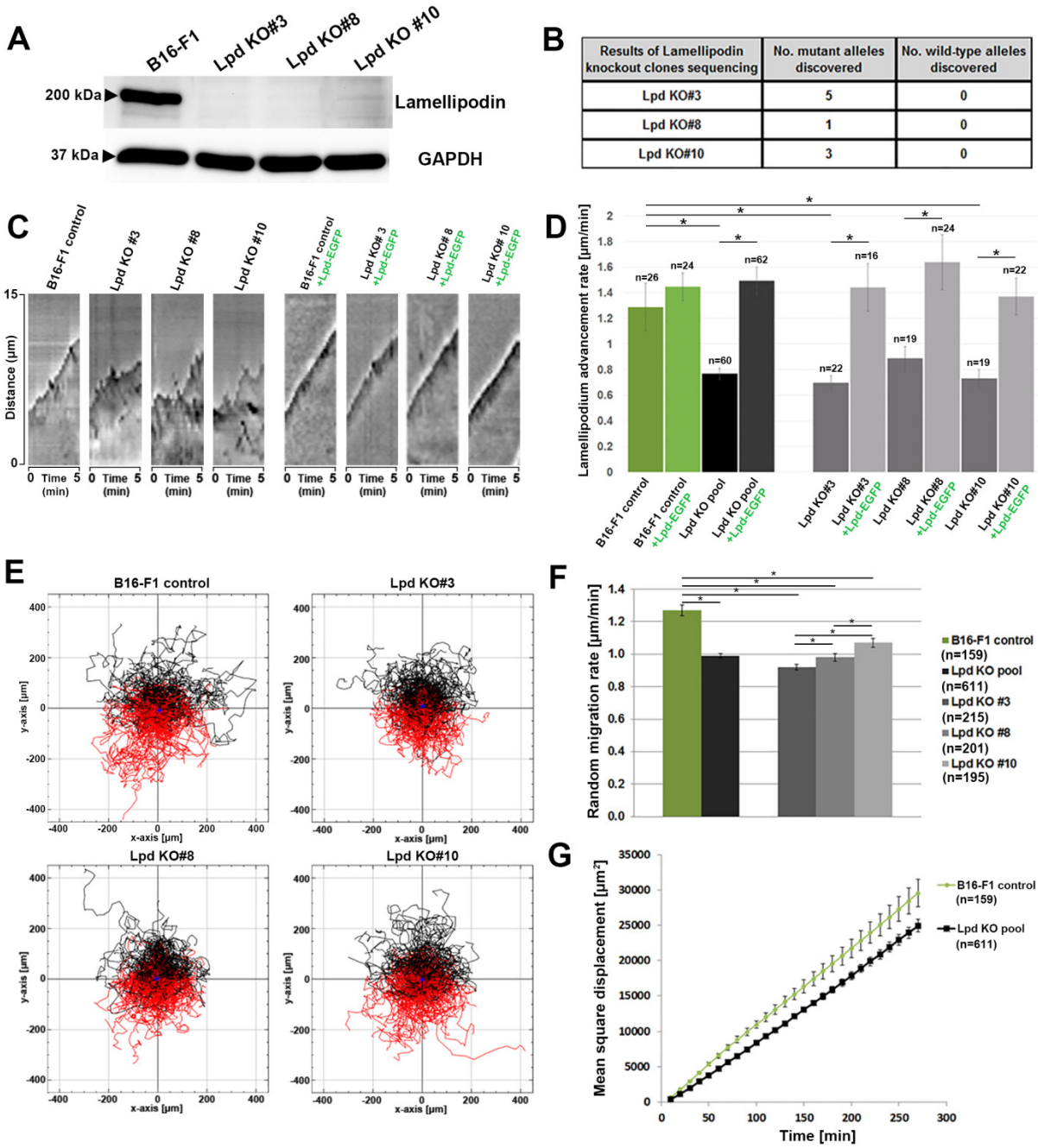

Fig. 2

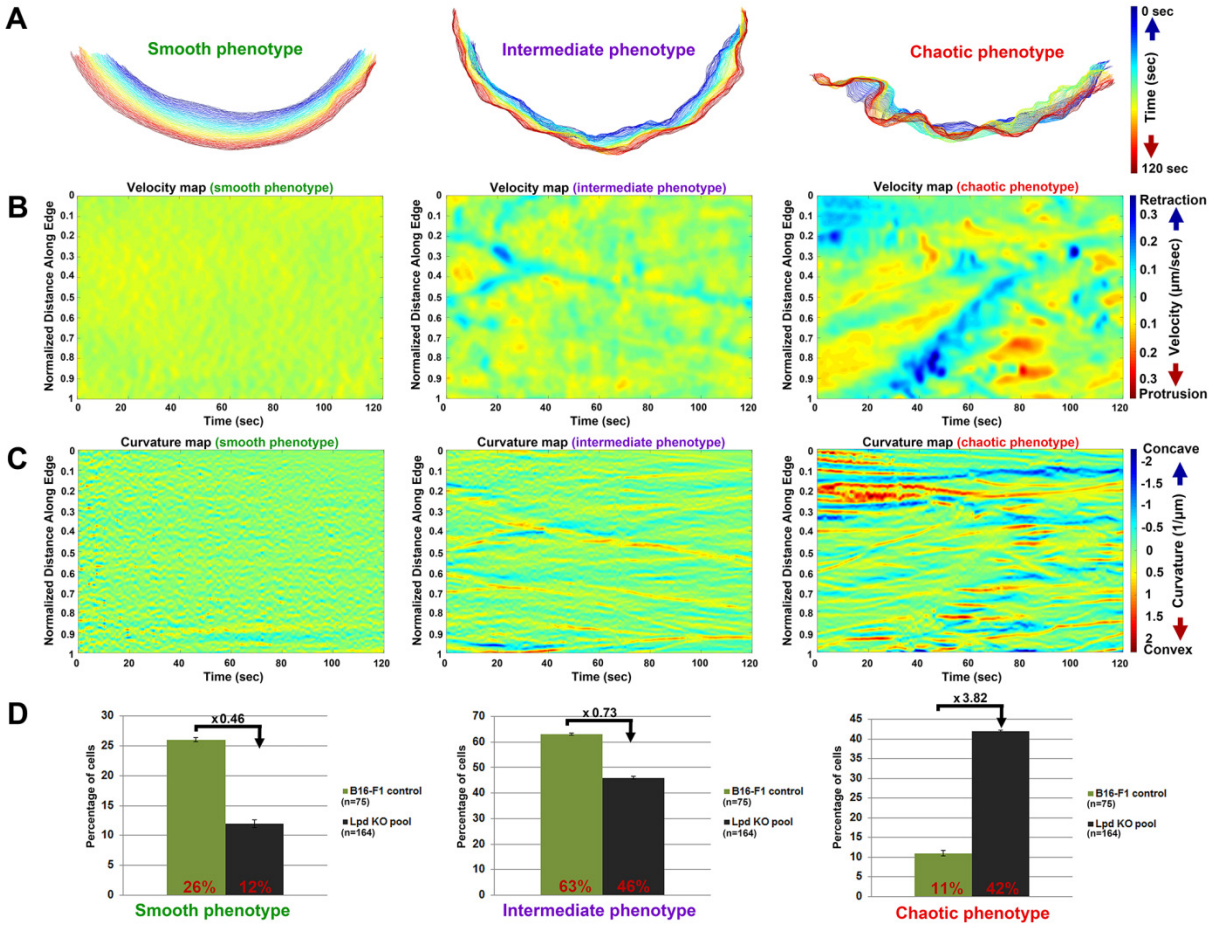

Fig. 3

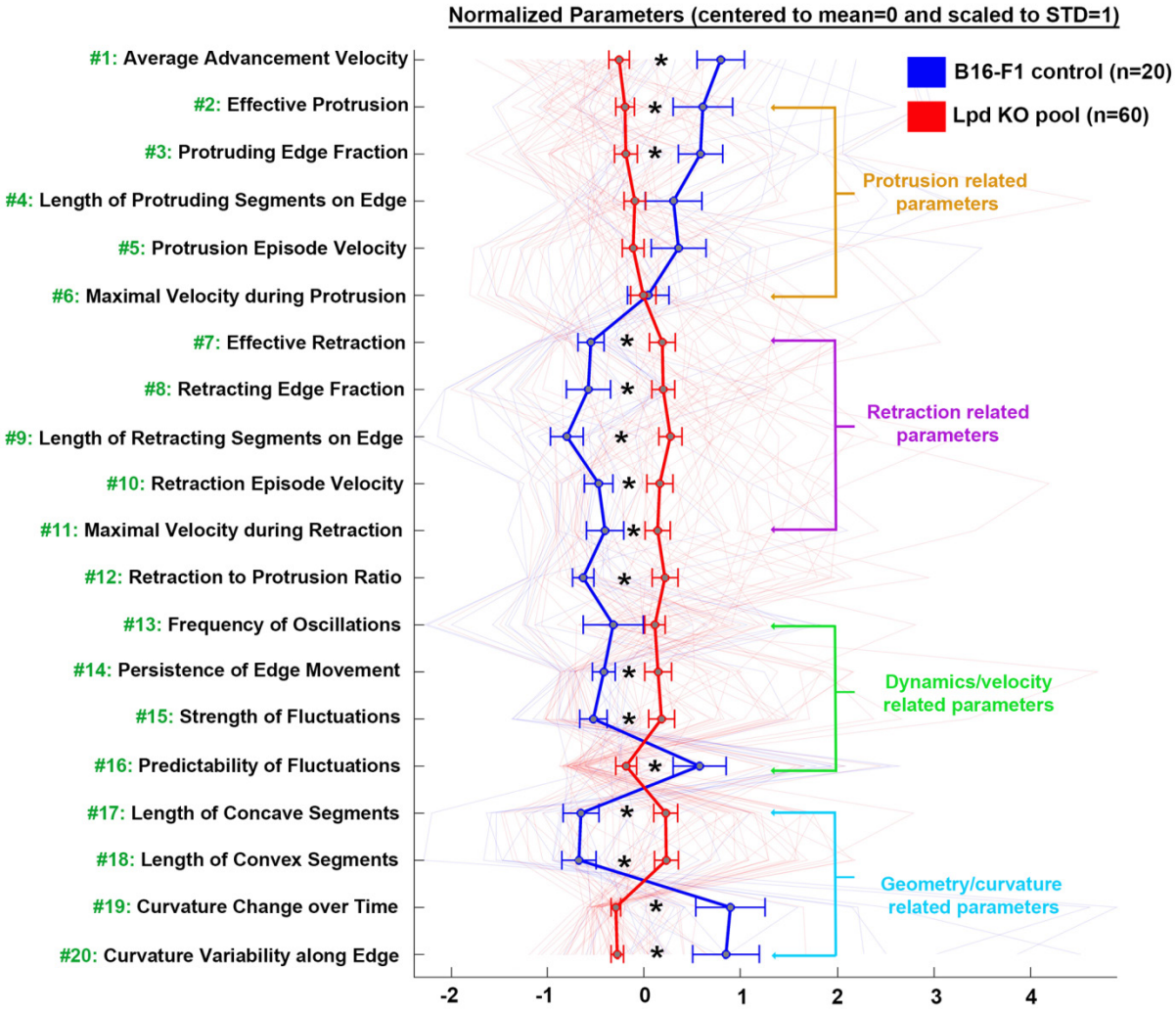

Fig. 4

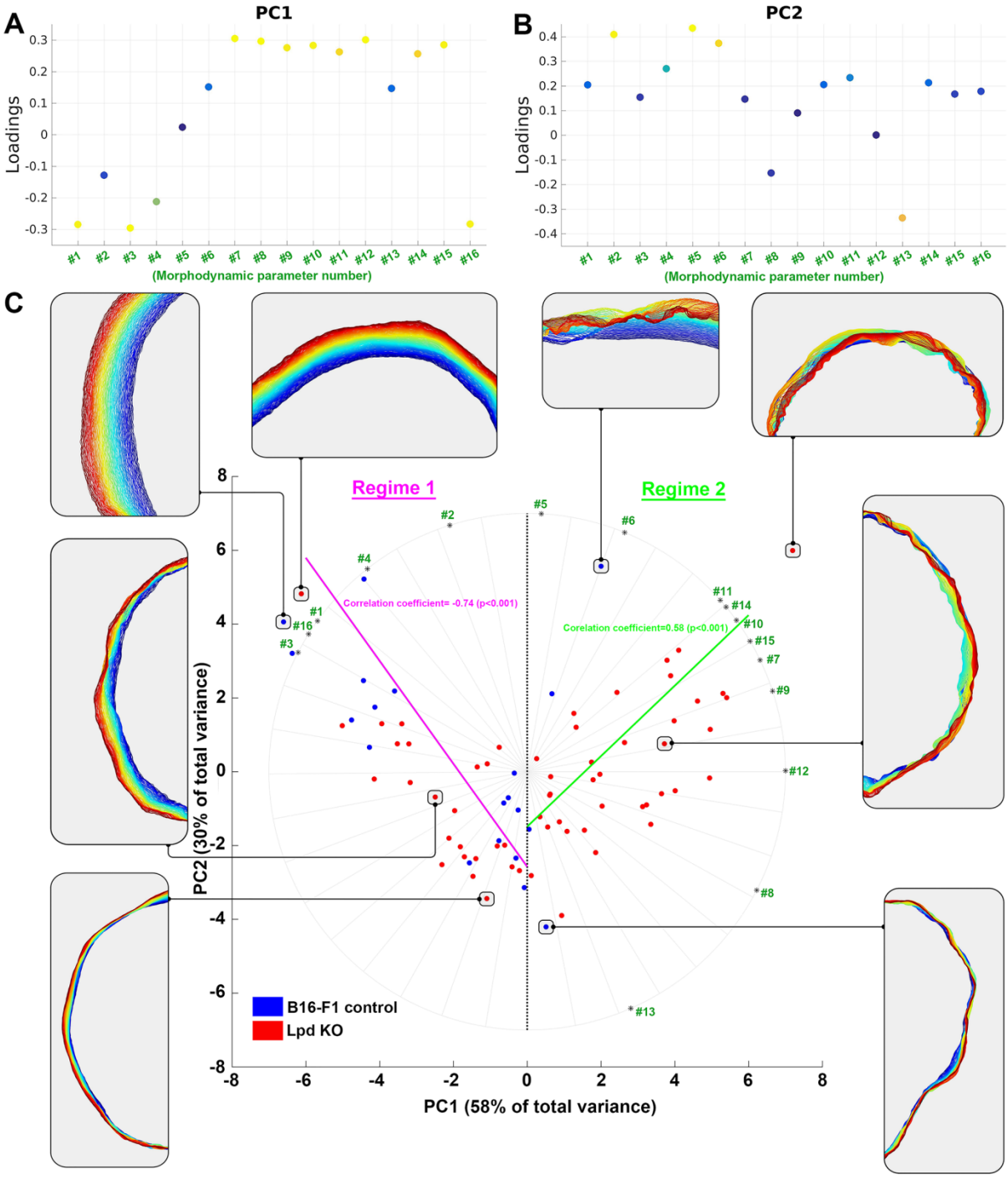

Fig. 5

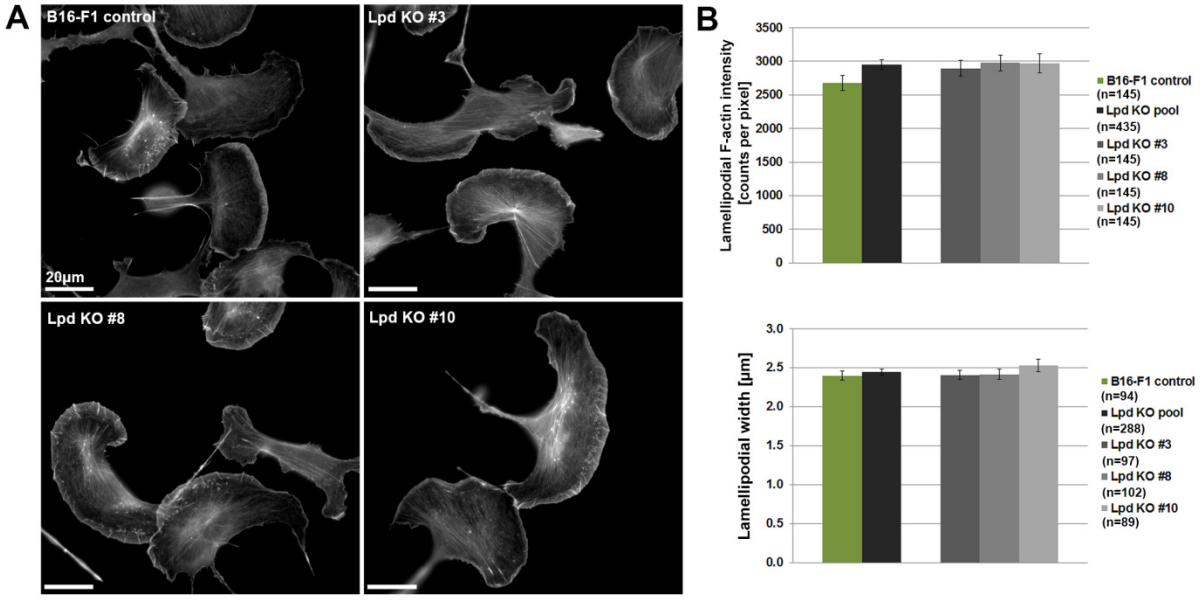

Fig. 6

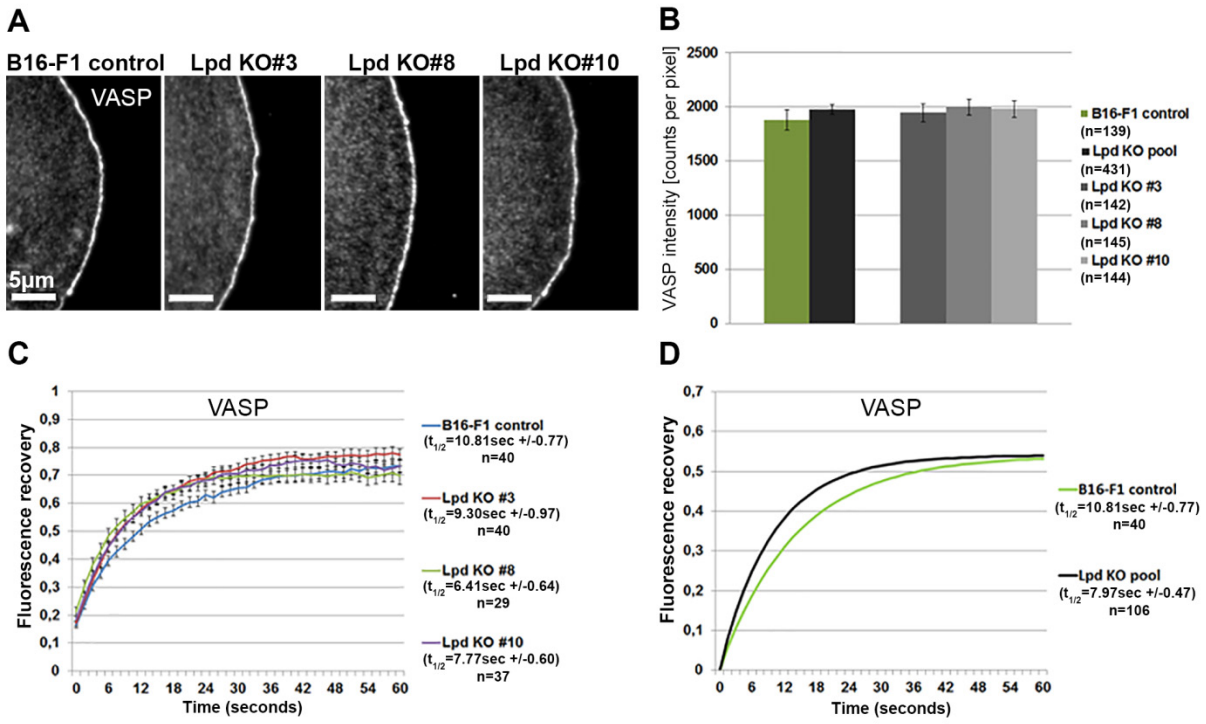

Fig. 7

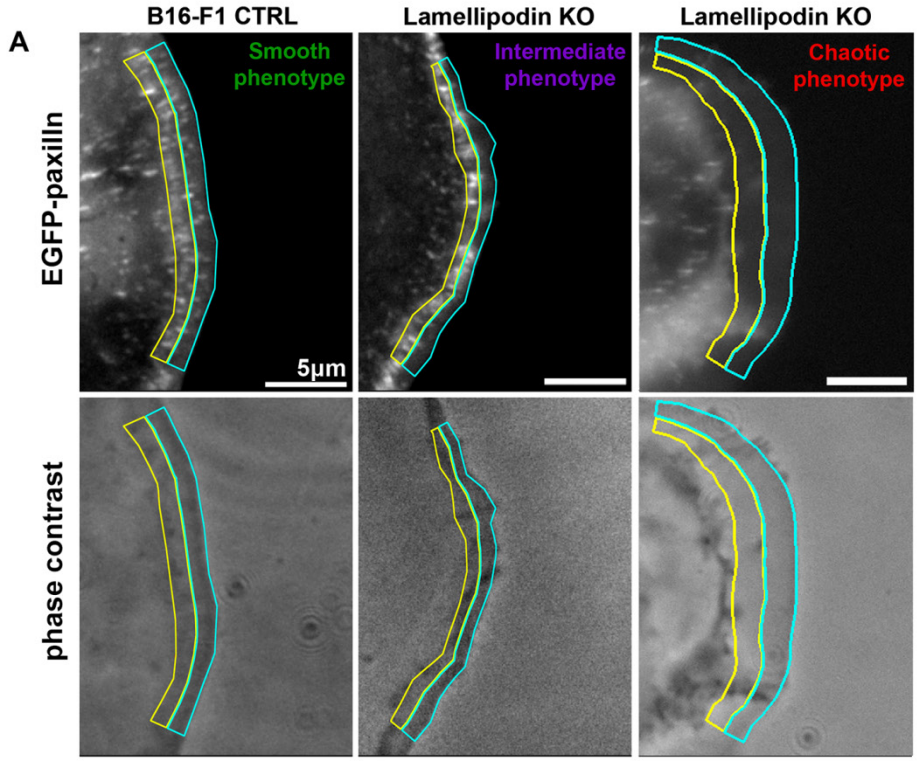

B

Lamellipodial protrusion phenotype	B16-F1 CTRL cell fraction for each phenotype (from 100%)	Lpd KO cell fraction for each phenotype (from 100%)	Ratio of Lpd KO: B16-F1 CTRL
Smooth phenotype	46%	20%	0.43
Intermediate phenotype	33%	30%	0.91
Chaotic phenotype	21%	50%	2.38

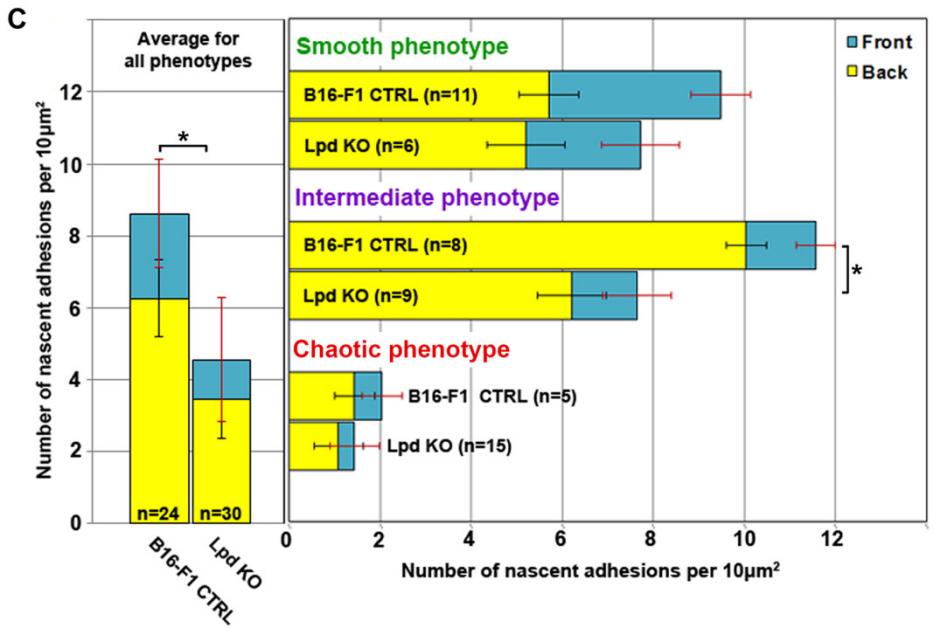

Fig. 8

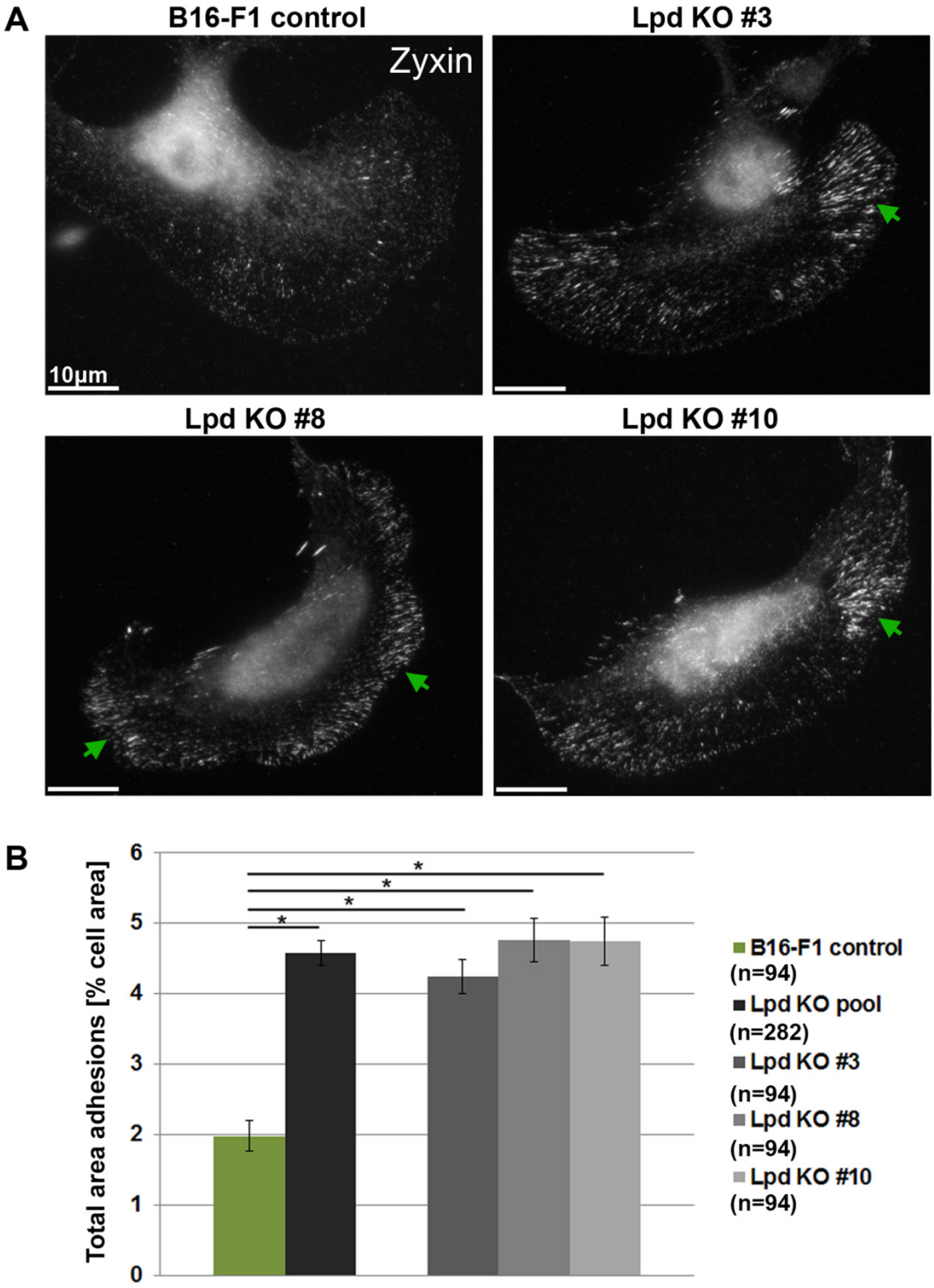

Fig. 9

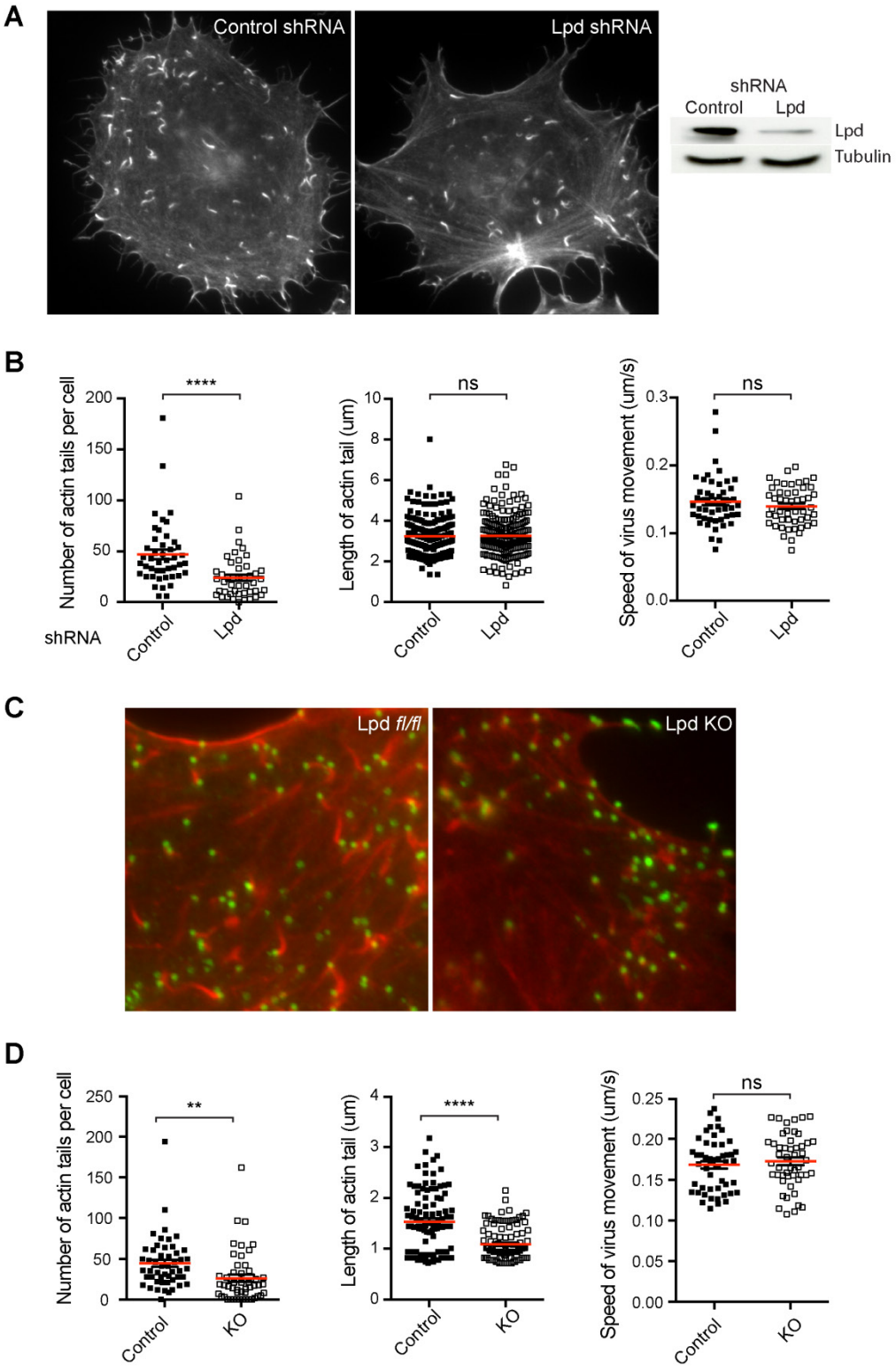

SUPPLEMENTARY MATERIAL

SUPPLEMENTARY FIGURE LEGENDS

Fig. S1. Confirmation of lack of Lpd expression in Lpd KO lines as well as of RIAM/PREL1. (A, B) Immunoblots with extracts from wildtype and Lpd KO cell lines using two alternative Lpd antibodies, as indicated; GAPDH was used as loading control. Note the absence of detectable Lpd protein levels in all characterized, independently generated knockout clones (Lpd KO#3, -#8 and -#10). (C) Immunolabellings using Lpd antibodies and counterstaining with phalloidin (insets) in distinct, indicated cell lines. White arrows point at clear accumulation of Lpd at the front edge of the lamellipodium in B16-F1 control cells, as expected, a staining pattern completely absent in representative cells shown for each KO cell population, in spite of the presence of a clear lamellipodium in each case (see phalloidin insets, Phall). (D) Immunoblot with RIAM/PREL1-specific antibody using lysates from NIH3T3 fibroblasts or B16-F1 cells, either untransfected or transfected with an untagged version of full-length PREL1. No detectable protein expression was observed in B16-F1 wild-type cells, as opposed to NIH3T3 or respective cells overexpressing PREL1 protein. Ponceau red staining was used as loading control (not shown). (E) Immunoblotting of B16-F1 wildtype and derived Lpd KO clones to test for potential upregulation of expression of RIAM/PREL-1 upon Lpd removal. However, at best a very faint band at expected molecular weight (115kDa) was detectable in all cell lines tested. A non-specific cross-reaction of the antibody was used as loading control.

Fig. S2. Morphodynamic protrusion analysis with wildtype and characterized Lpd knockout clones displayed individually. Data displayed as described for Fig. 3, except that knockout clones are displayed separately.

Fig. S3. Protrusion/retraction correlation analysis and assessment of lamellipodial actin assembly or Arp2/3 and Mena intensities.

(A) B16-F1 cells grouped into the three lamellipodial protrusion categories defined in Fig. 2 were plotted into a 2D-coordinate system with values for maximal velocity during protrusion and maximal velocity during retraction displayed on x- and y-axis, respectively. B16-F1 and Lpd KO cells were pooled for this analysis, and the data reveal a statistically significant, positive correlation between the two parameters. (B-D) Correlation analyses as described in A, but with protrusion categories displayed separately, as indicated. Note the absence of a statistically significant correlation in the smooth protrusion phenotype, caused perhaps by the great variability and/or low frequency of retraction events in this category. All data are arithmetic means +/- SEM. n equals number of individual movies and cells analysed. (E, F) Rates of actin network polymerization in the lamellipodium as assessed by FRAP of ectopically expressed, EGFP-tagged beta-actin in B16-F1 control or Lpd knockout cells, as indicated (E). Quantitation of Lpd KO results is either displayed individually or as pooled population (F). n equals number of cells analysed. One out of three Lpd KO clones (#10) appeared to display even a slight, but statistically significant increase in lamellipodial actin assembly rate (* = $p<0.05$), but this clonal variability was eliminated in the KO pool population. (G) Immunostaining and (H) quantitation of Arp2/3 complex (subunit p16A/ArpC5A) in B16-F1 control and Lpd knockout cells, as indicated. n=number of cells analysed, and data are arithmetic means +/- SEM. Statistics revealed no significant differences between any pair of experimental groups (not shown). (I) Immunostaining and (J) quantitation of Mena intensity at the lamellipodium edge in B16-F1 control and Lpd KO cells,

as indicated. In spite of moderate clonal variability among individual Lpd KO clones, no statistically significant differences between genotypes were found (not shown).

Fig. S4. Lpd-KO increases lamellipodial Abi-1 accumulation and reduces cell spreading. (A) Representative images of immunolabelling with Abi antibody at lamellipodia edges of B16-F1 control and Lpd knockout cells, as indicated. (B) Quantitation of lamellipodial Abi intensities in B16-F1 wildtype *versus* Lpd knockout cells. Data are arithmetic means +/- SEM, asterisks above bar charts indicate statistically significant differences between experimental groups, $p<0.05$, n equals number of cells measured. (C) Averaged raw data of fluorescent recovery curves after photobleaching of EGFP-tagged Abi-1, plotted for B16-F1 cells and all three individual Lpd KO clones. Determined half-times of recovery ($t_{1/2}$, in seconds, as derived from fitted data, see D and data not shown) for each group are displayed on the right, n equals number of FRAP movies used. (D) Curve fits of averaged, fluorescent recovery data of photobleached, lamellipodial Abi expressed in B16-F1 wildtype *versus* Lpd KO cells (all lines pooled for the latter). Derived half-times of recovery are displayed on the right, confirming the absence of any significant difference in Abi turnover rates between distinct cell types. (E-H) Western blots with total protein lysates using antibodies specific for VASP (E) or the WRC subunits Abi-1 (F), Nap1 (G), and WAVE2 (H). Equal loadings were controlled in each case by Ponceau S staining (not shown), and antibodies specific for vinculin or β-actin, as indicated. (I, J) B16-F1 wild-type cells or Lpd KO clones were seeded onto fibronectin (I) or laminin (J) for time periods of 15, 60 or 180 min, as indicated, fixed and quantified for cell area covered. Note the statistically significant reduction in cell area in the Lpd KO cell pool as compared to controls observed upon 15 or 60 min of spreading on fibronectin (I). The same trend was also observed after seeding on laminin, albeit less pronounced and not in a statistically significant fashion for the Lpd KO cell pool (J). Irrespective of substratum, this phenotype appeared to be compensated for upon extended

spreading periods (180 min). Data are arithmetic means +/- SEM, and single asterisks above bar charts show statistically significant differences between designated groups (* = $p<0.05$); n equals numbers of cells measured.

Fig. S5. Lpd localisation below Vaccinia virus and lack of effects on extracellular virus positioning and actin machinery recruitment. (A) Immunofluorescence images showing that both EGFP-tagged and endogenous Lpd (green) are recruited to the tip of actin tails (red) induced by Vaccinia virus (blue) in infected HeLa cells. (B) Immunofluorescence images reveal that after shRNA treatment of Hela cells, small amounts of endogenous Lpd (red) can still be observed at the tips of actin tails (green). Note this localisation can only be observed upon significant enhancement of fluorescence intensity post imaging ("high exposure"). (C) Quantification of number of extracellular virus per cell (n=30), and percentage of extracellular virus inducing an actin tail (n=30), in control and Lpd shRNA-treated cells. (D) Immunofluorescence images reveal the presence of endogenous core actin assembly factors on Vaccinia surfaces, Nck, N-WASP as well as the Lpd-ligand VASP (green) at the tips of vaccinia-induced actin tails (red-phalloidin), in control (Lpd *fl/fl*) and Lpd knockout MEFs (KO).

SUPPLEMENTARY TABLE

Table S1.

No.	Parameter name	Parameter description and biological relevance
1	Average Advancement Velocity	Parameter is equivalent to performing individual kymograph-based analyses of protrusion (as in Figure1C, D) on multiple points along the cell edge, thus subtracts retraction from protrusion rates at all points of the analyzed edge. If protrusion and retraction activities for each point were identical, the value of this parameter would be 0.
2	Effective Protrusion	Average protrusion velocity of all points considering the entire measurement period.
3	Protruding Edge Fraction	Average fraction of the edge protruding at any time during the period of measurement, expressed between 0 and 1, i.e. 1 representing the entire edge measured.
4	Length of Protruding Segments on Edge	Average length (in µm) of all protruding segments on measured edge. As opposed to parameter #3, where the average fraction of measured edge is calculated, this parameter defines average lengths of protruding segments over time.
5	Protrusion Episode Velocity	Average protrusion velocity of all points, considering only protrusive time periods.
6	Maximal Velocity during Protrusion	Corresponds to parameter # 5 in the highest quartile (top 25%).
7	Effective Retraction	Average retraction velocity of all points considering the entire measurement period.
8	Retracting Edge Fraction	Average fraction of the edge retracting at any time during the period of measurement, expressed between 0 and 1, i.e. 1 representing the entire edge measured.
9	Length of Retracting Segments on Edge	Average length (in µm) of all retracting segments on measured edge. As opposed to parameter #8, where the average fraction of measured edge is calculated, this parameter defines average lengths of retracting segments over time.
10	Retraction Episode Velocity	Average retraction velocity of all points, considering only retracting time periods.
11	Maximal Velocity during Retraction	Corresponds to parameter # 10 in the highest quartile (top 25%).
12	Retraction to Protrusion Ratio	This parameter is defined as the ratio of “Effective Retraction” (#7) over “Effective Protrusion” (#2). Values above 1 indicate retraction prevailing over protrusion.
13	Frequency of Oscillations	Frequency of oscillations/switches corresponds to the inverse of average time interval between consecutive velocity direction changes of each point along the measured edge (protrusion to retraction or *vice versa*).
14	Variance of Edge Acceleration	Reflects the variance of velocity changes as determined for all points along measured edge in all time frames. If the measured cell edge protrudes/retracts with equal velocities in all time frames (i.e. acceleration is zero), the parameter will be 0.
15	Strength of Fluctuations	Average of peak to peak amplitude of velocity oscillations of all points on the cell edge. The value for each point is calculated by averaging the velocity amplitude of all oscillation events of the point. This parameter thus defines the strength of velocity fluctuations at the cell edge irrespective of their direction.
16	Predictability of Fluctuations	Obtained by calculating average values of absolute, normalized autocorrelation of velocity over time and along edge performed to explore repetitive patterns. Parameter allows distinguishing between regular, repetitive patterns and chaotic random behavior of cell edge dynamics.
17	Length of Concave Segments	The average length (in µm) of concave segments on measured edge.
18	Length of Convex Segments	The average length (in µm) of convex segments on measured edge.
19	Curvature Change over Time	Derived from the rate of change of curvature for all measured points along the edge over time, followed by calculating the variance of all of these rates.
20	Curvature Variability along Edge	Reflects the variance of curvature changes with respect to distance along the cell edge, so this parameter gives an estimate of the average rate of concave to convex (and *vice versa*) transitions along the cell boundary for each time frame. It thus constitutes a spatial value and not dynamic one.

SUPPLEMENTARY MOVIE LEGENDS

Supplementary Movie 1. Comparison of protrusion dynamics in control and Lpd-deficient B16-F1 cells. Phase-contrast movies of B16-F1 wildtype and Lpd knockout cells (Lpd KO#10) migrating on laminin. Note individual examples of Lpd knockout cells, the protrusion of which is characterized by a fluctuating, chaotic mode of lamellipodial dynamics (white arrows).

Supplementary Movie 2. Exemplary generation of a velocity map. A simulated contour (yellow line) consisting of multiple points is slowly protruding to the right (black arrow on top) while retracting and protruding fractions of the edge with differential timing and velocity (see colour-velocity bar on the left). The velocity map on the right is building up in temporal synchrony with contour movements, illustrating how cell edge movements correlate with the outcome of the velocity map.

Supplementary Movie 3. Exemplary generation of a curvature map. A map reflecting the spatiotemporal changes of curvature of a simulated contour (from convex to linear and concave, as shown on the colour bar on the left) is generated. Everything is as described for Supplementary Movie 2, except that instead of velocity, the curvature of each point on the simulated contour is now read out relative to its immediate neighbours, as detailed in Methods.

Supplementary Movie 4. Differential dynamics of nascent adhesions in cells displaying distinct protrusion phenotypes. B16-F1 control and Lpd KO cells were transfected with

EGFP-paxillin, and subjected to time-lapse microscopy during migration on laminin using fluorescence and phase contrast channels, as indicated. A representative B16-F1 control (left panel) is displayed as example for the smooth protrusion phenotype, whereas the middle and right panels show representative examples for nascent adhesion dynamics typically found in protruding cells exhibiting the intermediate and chaotic phenotype, respectively. Phase contrast images (bottom) allow the correlation of distinct protrusion phenotypes with differential adhesion dynamics. The smooth protrusion phenotype is commonly associated with generation of multiple, nascent adhesions, continuously developing distally from previous sets of adhesions during continuous protrusion. Subsets of each population of nascent adhesions then are continuously elongated and developed into mature adhesions. In the intermediate phenotype (middle panels), nascent adhesions are less continuously formed and concentrated at the rear edge of the lamellipodium, frequently coincident with sites of active membrane ruffling. The chaotic protrusion phenotype with its commonly collapsing lamellipodia (right panels) is characterised instead by strongly reduced frequency of nascent adhesion formation.

Supplementary Movie 5. Dynamics of EGFP-tagged, full length lamellipodin (EGFP-Lpd) in a migrating B16-F1 cell. B16-F1 control melanoma cells expressing EGFP-Lpd and subjected to fluorescence and phase contrast time-lapse microscopy during its migration on laminin. Note the restriction of EGFP-Lpd localization to the edges of protruding and rearward ruffling lamellipodia, but the lack of association with nascent or mature focal adhesions.

Fig. S1

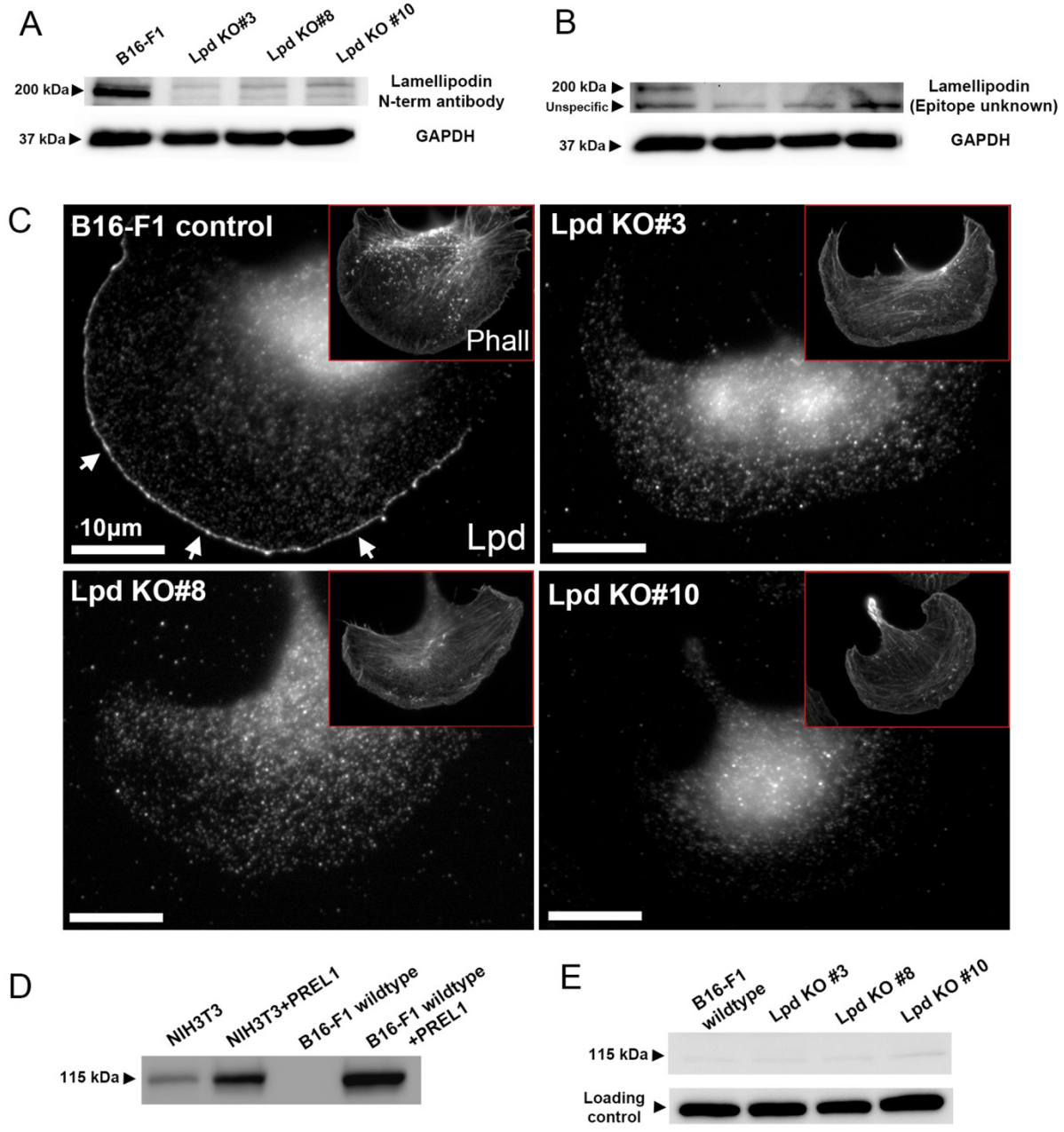

Fig. S2

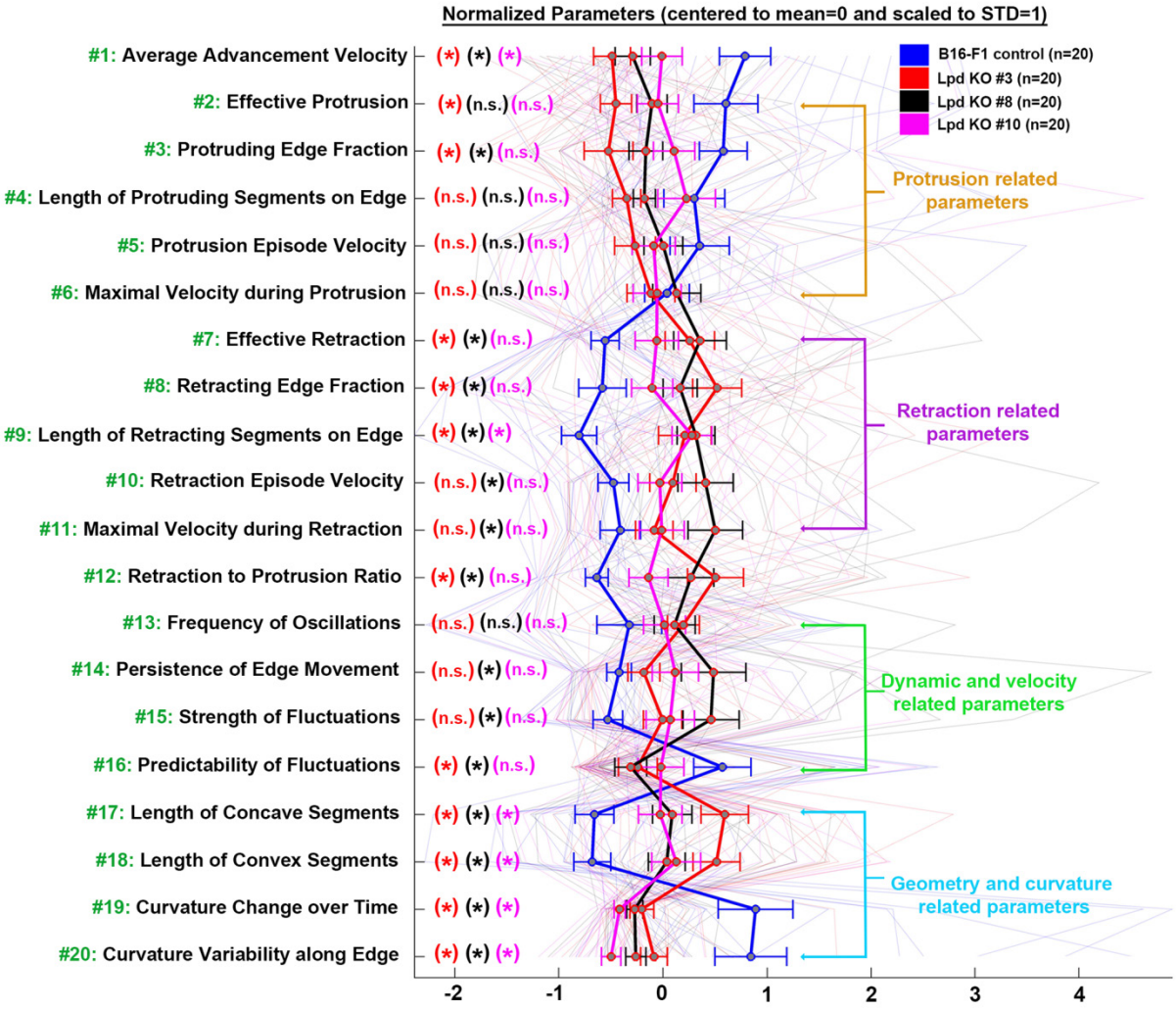

Fig. S3

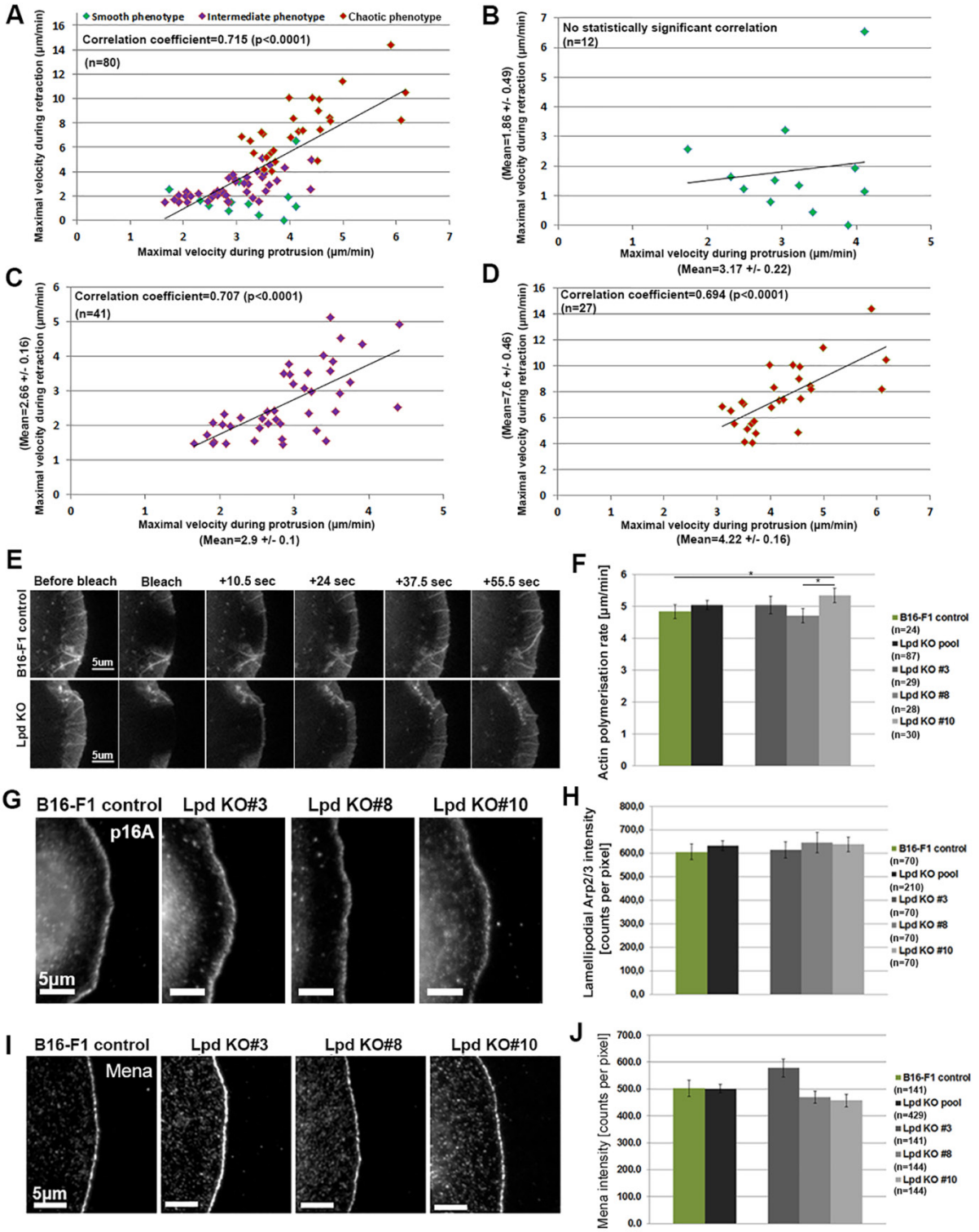

Fig. S4

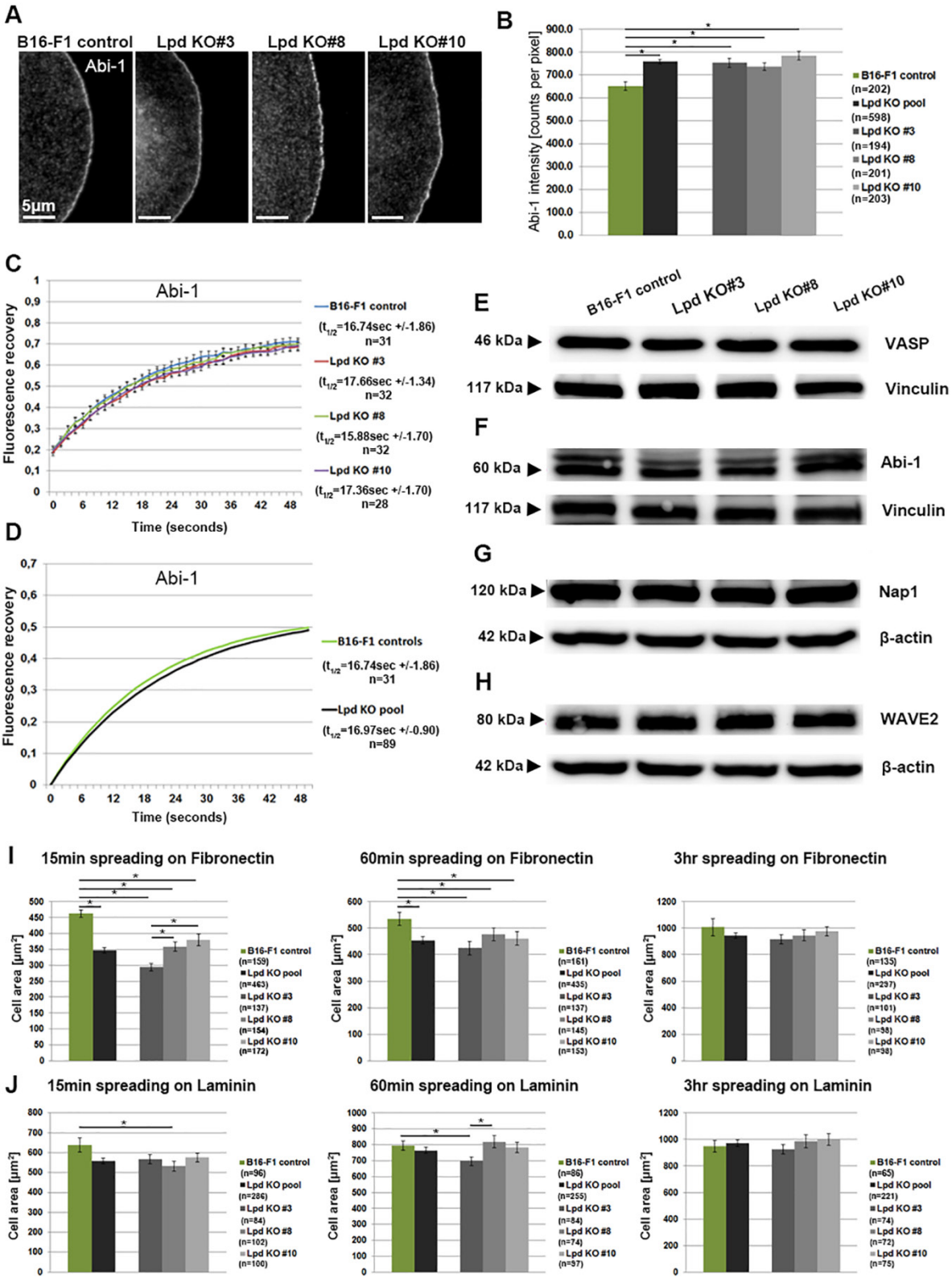

Fig. S5